

Heterogeneous Oceanic Arc Volcanic Rocks in the South Qilian Accretionary Belt (Qilian Orogen, NW China)

Liming Yang¹, Shuguang Song ^{1*}, Li Su², Mark B. Allen³,
Yaoling Niu^{2,3}, Guibin Zhang¹ and Yuqi Zhang¹

¹MOE Key Laboratory of Orogenic Belt and Crustal Evolution, School of Earth and Space Sciences, Peking University, Beijing 100871, China; ²Institute of Earth Sciences, China University of Geosciences, Beijing 100083, China; ³Department of Earth Sciences, Durham University, Durham DH13LE, UK

*Corresponding author. E-mail: sgsong@pku.edu.cn

Received June 5, 2018; Accepted November 19, 2018

ABSTRACT

Primitive arc magmas in oceanic island arcs are probes of sub-arc magmatic processes and are crucial for understanding oceanic subduction. We report data for an Early Paleozoic oceanic arc volcanic complex in the Lajishan–Yongjing terrane, South Qilian Accretionary Belt (SQAB), Qilian Orogen, including zircon U–Pb dating and Hf–O isotopes, mineral and whole-rock geochemistry, and Sr–Nd isotope compositions. New zircon ages of ~455–440 Ma constrain the timing of arc volcanism and the subduction of the Qilian Ocean. Based on petrography and bulk-rock composition, five lithological types have been identified: ankaramite; high-Mg basaltic andesite; high-Al andesite; boninite; sanukite. The volcanic sequence thus is one of the few island arcs where three types of near-primitive arc rocks including boninite, ankaramite and sanukite have been simultaneously produced. All these rocks have variably enriched Sr–Nd isotopic compositions, positive to slight negative zircon $\varepsilon_{\text{Hf}}(t)$ values and elevated zircon $\delta^{18}\text{O}$ values. Boninites, ankaramites and sanukites are interpreted as contemporary near-primitive melts generated from different sources and conditions within an island arc setting. Boninites are characterized by low Ti and REE concentrations and high Cr# chrome spinel, and are interpreted as melts of refractory, Cpx-poor, spinel lherzolite or harzburgite at >25% partial melting. Anomalous zircon $\delta^{18}\text{O}$ values of 6.57–7.61‰ and Sr–Nd mixing calculations suggest less than 2% incorporation of subducted oceanic sediments into the mantle source of the magmas. The ankaramites are characterized by low SiO₂ and high MgO (Mg#), Cr, Ni and La/Yb ratios, and have similar isotopic ratios to tectonically adjacent ocean island basalt (OIB) lavas. The ankaramite lavas are likely to have derived from mantle sources similar to those of OIB; that is, pyroxenite-bearing garnet peridotite enriched in incompatible elements. High-Mg basaltic andesites and high-Al andesites may be derived from parental ankaramite magmas. Sr–Nd–Hf isotopic mixing modeling constrains the amount of silicic melt to ~1–4% for ankaramite magma. Sanukites are of andesitic–dacitic composition with high Mg#, Cr and Ni, and enriched large ion lithophile elements and high La/Yb ratios. They are interpreted as having been generated by reaction of mantle peridotite with a silicic melt, itself derived from subducted sediments. Enriched Sr–Nd–Hf isotopic compositions constrain the amount of silicic melt to ~10–15% for sanukite. Large compositional variations among the volcanic rocks from the same arc reflect heterogeneous mantle sources and variable degrees of mantle metasomatism by sediment-derived hydrous fluids or silicic melts, accompanied by secondary assimilation–fractional crystallization processes during magma ascent to the surface. The generation of the island arc volcanic sequence in the Lajishan–Yongjing Terrane is a response to the collision between the Lajishan–Yongjing Oceanic Plateau (recorded by the Lajishan–Yongjing Ophiolite) and the pre-existing trench–continental margin. Evolution from a continental margin in the North Qilian Accretionary Belt to an oceanic island arc in the SQAB records subduction advance and retreat in the history of the Qilian Ocean.

Key words: intra-oceanic arc; ankaramite; boninite; sanukite; mantle metasomatism by subducted sediments; zircon Hf–O isotope; Qilian Orogen

INTRODUCTION

In the modern Earth, volcanic arc systems at convergent plate margins can be subdivided into (1) island arcs (e.g. Western Pacific-type Izu–Bonin–Mariana oceanic arc) and (2) continental arcs, according to the different types of overriding plate (Gill, 1981). If the overriding plate is oceanic, the resulting magmatism forms an island arc, possibly with primitive arc magmas, including primitive andesites (e.g. Kelemen *et al.*, 2003), arc picrites (e.g. Rohrbach *et al.*, 2005), island arc ankaramites (e.g. Barsdell & Berry, 1990) and boninites (e.g. Crawford *et al.*, 1989). If the overriding plate is continental, the resulting magmatism is typically more evolved, with calc-alkaline or alkaline rocks and fewer tholeiitic or low-K series volcanic rocks than island arcs (Miyashiro, 1974; Song *et al.*, 2013).

Erupted primitive magmas in island arcs are in principle probes of their sub-arc mantle sources (Falloon & Danyushevsky, 2000; Green *et al.*, 2004; Mitchell & Grove, 2015), providing direct evidence of sub-arc magmatic processes (Greene *et al.*, 2006). However, a major obstacle to our understanding of the sources of island arc magmas is the effect of crustal evolution on the volcanic products (Leeman, 1983). In this regard, primitive arc volcanic rocks are extremely useful, whether they occur in modern arcs or ancient island arcs preserved within continents by orogeny and accretion (e.g. Takashima *et al.*, 2002; Greene *et al.*, 2006; Stern *et al.*, 2012).

Subduction accretionary belts in continental orogens record ancient subduction and orogenic process by accretion of microcontinents, oceanic crust (e.g. oceanic plateaux, seamounts), arc magmatic complexes and finally continent–continent collision. The most abundant petro-tectonic assemblage preserved in accretionary orogens is dominated by the continental arc, with subordinate oceanic terranes (arcs, crust, mélange, large igneous provinces, etc.) and older, reworked crust (Condie, 2014). As most of the juvenile crust in orogens is found in continental arc assemblages produced during closure of the ocean basin, subduction accretionary belts play an important role in directly understanding continental growth and assembly in Earth's history (Cawood *et al.*, 2009).

The Lajishan–Yongjing Terrane in the middle part of the South Qilian Accretionary Belt is an Early Paleozoic subduction accretionary belt, formed by accretion of ophiolite and island arc volcanic complexes, and intrusion of arc-related plutons (Yang *et al.*, 2002; Xiao *et al.*, 2009; Yan *et al.*, 2012, 2015; Fu *et al.*, 2014; Wang *et al.*, 2016; Song *et al.*, 2017; Zhang *et al.*, 2017). Ophiolites in this region are composed of picrites and ocean island alkaline and tholeiitic basalts, and have been demonstrated to be an oceanic plateau that was the product of

a mantle plume (Song *et al.*, 2017; Zhang *et al.*, 2017). As subduction proceeded, the oceanic plateau arrived at, then jammed the trench, and finally accreted to the existing continent as an ophiolitic component (Niu *et al.*, 2003, 2017). Thus, the accretionary complexes provide us with an opportunity to reveal the tectonic relationship between the collision of an oceanic plateau and the generation of an intra-oceanic arc volcanic complex.

In this study, we examine various rock types of island arc affinity from the Lajishan–Yongjing Terrane, and provide an integrated investigation of *in situ* zircon U–Pb dating and Hf–O isotopes, in combination with mineral and whole-rock chemistry and Sr–Nd isotopes. The aims are to (1) describe an Early Paleozoic oceanic arc embedded in an ancient continental orogenic belt, (2) characterize the magmatic processes forming the volcanic rocks, and place constraints on the nature of the parental magmas, (3) precisely date the volcanic rocks of the island arc complex, and (4) decipher its tectonic relationship with the collision between the Lajishan–Yongjing Oceanic Plateau and the Central Qilian Continental Margin.

GEOLOGICAL SETTING

The Qilian–Qaidam Orogenic Belt is a wide orogenic collage, with its width exceeding 300 km, at present located on the northern margin of the Tibetan Plateau and adjacent areas, including the Qaidam Basin to the south, the Tarim Basin to the NW, and the Alax block to the NE (Fig. 1a). It is offset by the Altyn Tagh fault in the west and merges with the East Kunlun Orogen to the east, and continues farther to the east merging with the Qinling–Dabie orogenic belt (Song *et al.*, 2013, 2017). This whole region consists of two subparallel oceanic-type accretionary belts and one continental-type ultra-high-pressure metamorphic (UHPM) belt, occurring between two Precambrian blocks. From north to south, the Qilian–Qaidam Orogenic Belt can be subdivided into five tectonic units: the North Qilian Accretionary Belt (NQAB), the Central Qilian Block, the South Qilian Accretionary Belt (SQAB), the Quanji–Oulongbuluke Block and the North Qaidam UHPM Belt (Fig. 1b; Song *et al.*, 2014).

The NQAB is an elongate, NW-trending orogenic belt that lies between the Alax Block (north) and the Central Qilian Block (south). It is offset by the strike-slip Altyn Tagh Fault for up to 400 km in the NW (Zhang *et al.*, 2001) and is bounded by the Longshoushan Fault to the Alax Block. This belt is considered as a material record of a typical early Paleozoic oceanic-type subduction zone that consists of two ophiolite suites with zircon U–Pb ages of 560–450 Ma, arc magmatic sequences

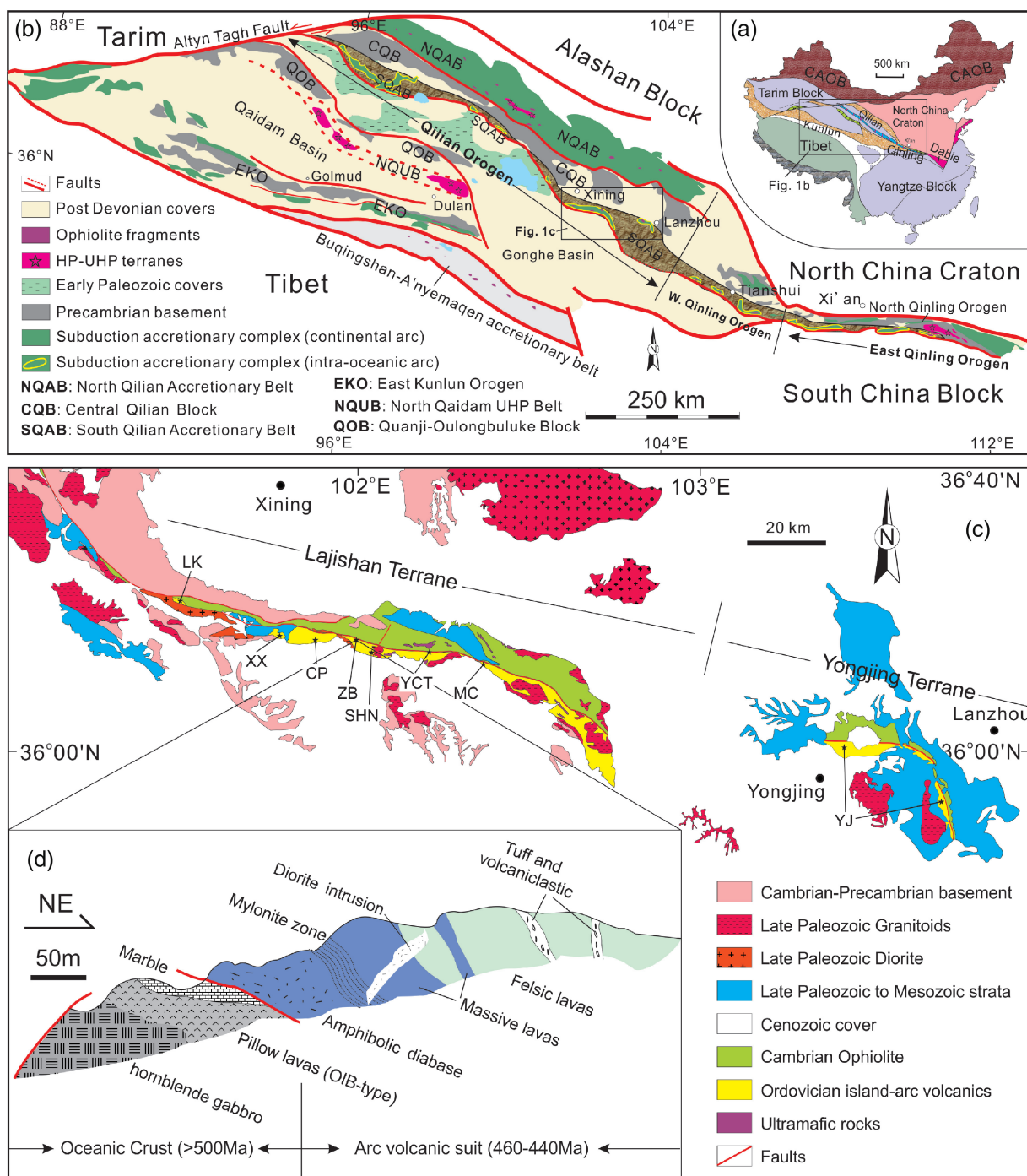


Fig. 1. (a) Schematic map showing the major tectonic units of China [modified after Song *et al.* (2017)]. CAOB, Central Asian Orogenic Belt. (b) Simplified geological map of the Central China Orogenic Belt [modified after Song *et al.* (2017)]. (c) Simplified geological map of the Lajishan–Yongjing Terrane showing sample locations: LK, Lajishankou; XX, Xiongxiang; CP, Chapu; ZB, Zhaba; SHN, Sihaning; MC, Machang; YCT, Yaocatai; YJ, Yongjing. (d) Zhaba cross-section of the Lajishan Terrane.

including intermediate–felsic volcanic rocks (510–450 Ma) and I-type granite or granodiorite plutons (510–420 Ma), and high-pressure–low-temperature (HP–LT) metamorphic rocks with metamorphic ages of 490–440 Ma (Wu *et al.*, 1993; Liu *et al.*, 2006; Song *et al.*, 2006, 2009, 2013; Zhang *et al.*, 2007). A boninitic sequence (517–490 Ma) in the back-arc setting was also reported by Xia *et al.* (2012).

The Central Qilian Block between the NQAB and the SQAB consists mainly of Paleoproterozoic granitic gneiss, leucogranite and rapakivi granites with Neoproterozoic granitic intrusions, which has affinities in the geochronological spectrum of magmatism and rock assemblages with the Yangtze Block (Wan *et al.*, 2001; Gehrels *et al.*, 2003; Tung *et al.*, 2007, 2013; Song *et al.*, 2010, 2012, 2014).

The SQAB occurs as discontinuous, NW–SE-oriented fault-bounded slivers along the south margin of Central Qilian Block, and is separated from the Quanjī–Oulongbuluke blocks by thick (more than 5 km) and wide (exceeding 100 km) Paleozoic sedimentary sequences (Song *et al.*, 2014). It mainly consists of, from NW to SE, the Yanchiwan Terrane, the Gangcha Terrane, the Lajishan–Yongjing Terrane and the Yongjing Terrane, and extends further east to the West Qinling and East Qinling, collectively forming the Qi–Qin Accretionary Belt (QQAB) with a total length of ~2000 km (Song *et al.*, 2017). The SQAB is composed of two sequences: a Cambrian to Ordovician ophiolite sequence and an Ordovician volcanic arc sequence (Song *et al.*, 2017; Zhang *et al.*, 2017). The ophiolites crop out to the north of the arc sequence and consist of massive and pillowed picrite, ocean-island tholeiitic and alkaline basalt with minor ultramafic rocks, gabbro and pelagic chert (Fu *et al.*, 2014; Zhang *et al.*, 2017). The arc-volcanic sequence is mainly composed of pillow metabasalt, volcanoclastic rocks and andesitic porphyry, which are imbricated with chert and minor carbonate (Xiao *et al.*, 2009). Silurian flysch occurs as fault-bounded slices within the accretionary complex. These rocks are unconformably overlain by Devonian molasse and Carboniferous to Triassic sedimentary cover.

ROCK ASSEMBLAGES

The SQAB arc-volcanic complex occurs in the southern part of the accretionary terranes in a NW–SE orientation with an area of ~200 km × 20 km (Fig. 1c). It is bounded by thrust faults with the ophiolite sequence, and is unconformably covered by Cretaceous strata. Samples were collected along the extension of the arc-volcanic complex within the Lajishan–Yongjing terrane (see Fig. 1c for sampling localities). A cross-section in Zhaba town (Fig. 1d) shows the relations of pillowed and massive basalt–andesite with layered dacitic lava and volcanoclastic rocks. The upper crust exposures are ocean island basalt (OIB)-type pillow lavas (>500 Ma), described by Zhang *et al.* (2017). The lower part of the arc suite (~460–440 Ma) is composed of a thick sequence of amphibole-rich diabase, intruded by diorite, and overlain by intermediate–basic volcanic rocks. The intermediate–basic volcanic rocks are dark-colored lavas, with massive or pillow structures, and are generally porphyritic, characterized by an essentially glassy groundmass with varying amounts of microlites (Fig. 2a and b). The upper part of the exposures of the arc suite is composed of thick sequences of light-colored lavas ranging from andesite to dacite overlain by tuff and volcanoclastic debris-flow deposits (Fig. 2c and d). Five types of lithologies can be recognized in the field based on their colour and structure: (1) dark-green-colored, pyroxene phenocryst-rich basalt–andesite (ankaramite); (2) dark-green-colored, phenocryst-poor basaltic andesite with pillow and massive structures (boninite and high-Mg basaltic andesite) (Fig. 2a); (3) reddish andesite

with plagioclase phenocrysts (high-Al andesite) (Fig. 2b); (4) white- or grey-colored dacite with Pl and/or Qtz phenocrysts (mostly sanukite) (Fig. 2c); (5) volcanic breccia (Fig. 2d).

ANALYTICAL METHODS

Bulk-rock major and trace element analyses

Bulk-rock major and trace element analyses were carried out at the China University of Geosciences, Beijing (CUGB); detailed analytical procedures have been reported previously by Song *et al.* (2010). Bulk-rock major element compositions were determined using inductively coupled plasma atomic emission spectroscopy (ICP-OES). The analytical uncertainties are generally less than 1 wt % for most elements with the exception of TiO₂ (~1.5%) and P₂O₅ (~2.0%) based on rock standards GSR-1 and GSR-3 (national geological standard reference material of China), AGV-2 and W-2 (US Geological Survey; USGS). Loss on ignition (LOI) was determined by placing 1 g of sample in a furnace at 1000°C for 3 h before being cooled in a desiccator and re-weighed. The trace element analyses were made by inductively coupled plasma mass spectrometry (ICP-MS) using an Agilent-7500a system. About 50 mg of powder of each sample was dissolved in an equal mixture of distilled HF and HNO₃ in Teflon digesting vessels and heated at 195°C for 48 h using high-pressure bombs for digestion. The sample was then evaporated to incipient dryness, refluxed with 1 ml of 6N HNO₃ and heated again. The sample was again dissolved in 2 ml of 3N HNO₃ and heated at 165°C for a further 24 h to guarantee complete dissolution. Finally, it was diluted with Milli-Q water (18MΩ) to a dilution factor of 2000 in 2% HNO₃ solution for analysis. Rock standards AGV-2, W-2, and BHVO-2 (USGS) were used to monitor the analytical accuracy and precision. The analytical accuracy, as indicated by relative difference between measured and recommended values, is better than 5% for most elements, and 10–15% for Cu, Sc, Nb, Ta, Er, Tm, Gd Th, and U.

Mineral chemistry

In situ mineral analyses for major element oxides, including clinopyroxene (Cpx) and spinel, were made using a JEOL JXA-8100 electron probe micro analyzer (EPMA) at Peking University. Analytical conditions were optimized for standard silicates and oxides at 15 kV accelerating voltage with a 20 nA focused beam current for all the elements. *In situ* mineral analyses for trace elements in Cpx were made by laser ablation (LA)-ICP-MS using an Agilent-7500a system coupled with a New Wave UP-193 solid-state LA system in the Geological Laboratory Center, CUGB. Routine analyses were obtained by counting for 30 s at peak and 10 s on background. Repeated analysis of natural and synthetic mineral standards yielded precisions better than ±2% for most elements.

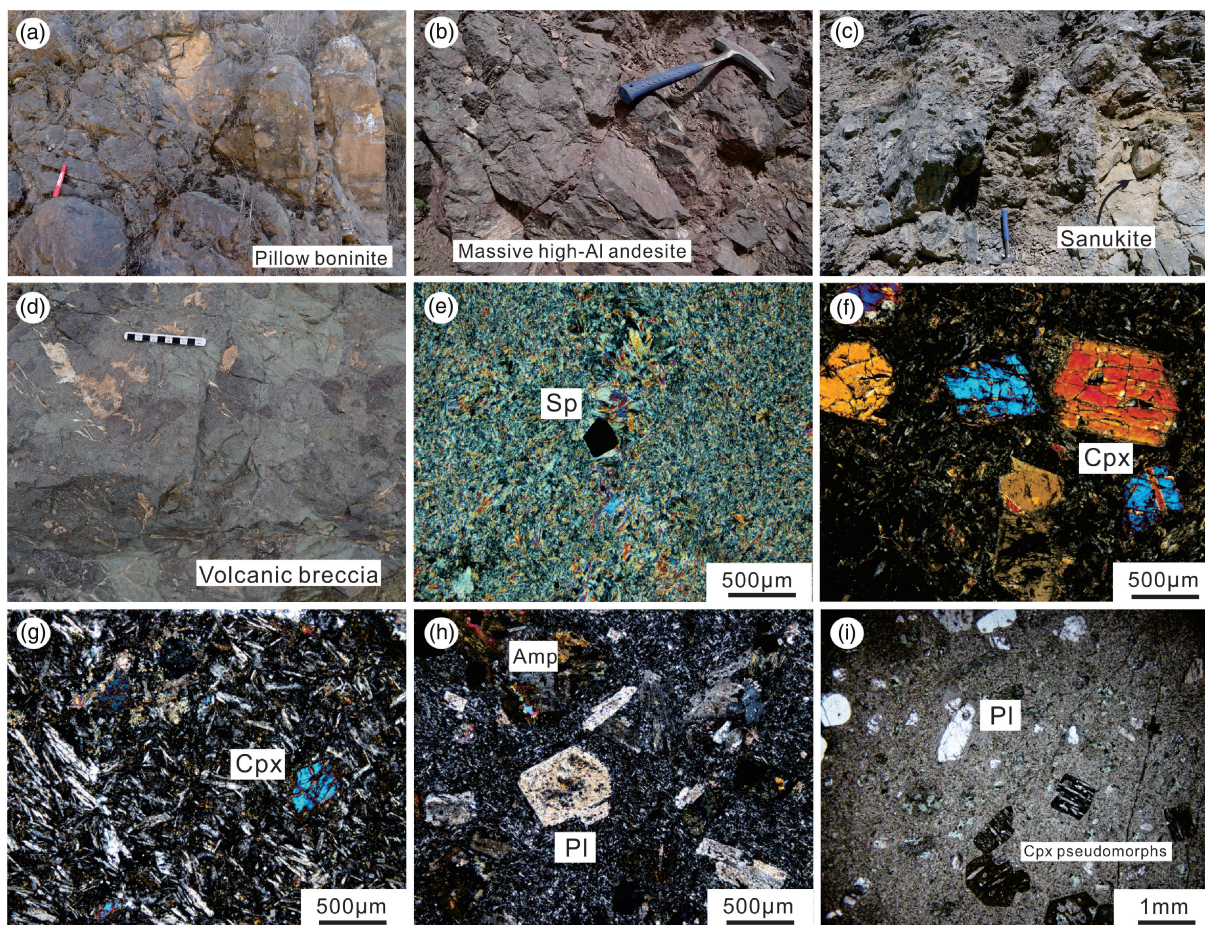


Fig. 2. Representative field photographs and microphotographs of island arc volcanic rocks from the Lajishan–Yongjing Terrane: (a) pillow boninite; (b) reddish, massive andesite with plagioclase phenocrysts; (c) dark-colored intermediate–basic lavas overlain by light-colored felsic lavas (sanukite); (d) volcanic breccia; (e) boninite (sample LJ15-12); (f) ankaramite (sample 13QLS-71); (g) high-Mg basaltic andesite (sample LJ15-40); (h) high-Al andesite (sample LJ15-18); (i) sanukite (sample 12LJ-13). Cpx, clinopyroxene; Sp, spinel; Pl, plagioclase.

Bulk-rock Sr–Nd isotope analyses

Separation and purification of Sr–Nd were carried out using conventional two-column ion exchange procedures in the ultraclean laboratory of the MOE Key Laboratory at Peking University. About 300 mg of unknown sample and ~200 mg of standard sample (BCR-2) were dissolved in a mixture of HF + HNO₃ in Teflon vessels and heated at 140°C for 7 days for complete dissolution. The pure Sr and Nd were separated from the remaining solution by passing through conventional cation columns (AG50W and P507) and the detailed ion exchange procedures include (1) separation of Sr and light rare earth elements (LREE) through a cation-exchange column (packed with 200 mesh AG50W resin) and (2) purification of Nd through a second cation-exchange column (packed with 200 mesh P507 resin). The bulk-rock Sr–Nd isotope analyses were performed by multi-collector inductively coupled plasma mass spectrometry (MC-ICP-MS) at the MOE Key Laboratory of Orogenic Belts and Crustal Evolution, Peking University. The ⁸⁷Rb/⁸⁶Sr and ¹⁴⁷Sm/¹⁴⁴Nd ratios were calculated based on Rb, Sr, Sm, and Nd contents

determined by ICP-MS (CUGB). Mass fractionation corrections for Sr and Nd isotopic compositions were normalized to ⁸⁶Sr/⁸⁸Sr = 0.1194 and ¹⁴⁶Nd/¹⁴⁴Nd = 0.7219, respectively. All ⁸⁷Sr/⁸⁶Sr ratios have been adjusted against Sr standard NBS-987 Sr = 0.710250 and the reported ¹⁴³Nd/¹⁴⁴Nd ratios were further adjusted relative to the JNdi-1 standard of 0.512115. Initial ¹⁴³Nd/¹⁴⁴Nd ratios and corresponding $\epsilon_{Nd}(t)$ values were calculated on the basis of present-day reference values for CHUR: (¹⁴³Nd/¹⁴⁴Nd)_{CHUR} = 0.512638 and (¹⁴⁷Sm/¹⁴⁴Nd)_{CHUR} = 0.1967 (Jacobsen & Wasserburg, 1980). Rock standard BCR-2 was used to evaluate the separation and purification process of Rb, Sr, Sm, and Nd. Repeated analyses for the Nd and Sr standard samples (JNdi and NBS987) yielded ¹⁴³Nd/¹⁴⁴Nd = 0.512197 ± 11 (2σ, n = 7) and ⁸⁷Sr/⁸⁶Sr = 0.710229 ± 11 (2σ, n = 7), respectively.

Zircon U–Pb dating analysis

Zircons were separated by using standard density and magnetic separation techniques. Zircon grains were embedded in an epoxy mount and then polished to

expose the inner structure for analysis. Cathodoluminescence (CL) images were acquired to observe the internal structures of zircon grains, using a CL spectrometer (Garton Mono CL³⁺) on a Quanta 200F environmental scanning electron microscope at scanning conditions of 15 kV and 120 nA in the School of Earth and Space Sciences, Peking University.

Measurements of U–Th–Pb isotopes for samples LJ15-01 and LJ15-70 were conducted by secondary ion mass spectrometry (SIMS) using a Cameca IMS-1280 system at the Institute of Geology and Geophysics, Chinese Academy of Sciences, Beijing. The U–Pb dating analyses were conducted after the O isotope analyses and obtained from the same domain. Before the U–Pb dating analyses, the mounted zircons were carefully re-ground and re-polished. The analytical procedures are similar to those reported by Li *et al.* (2010a, 2010b). The O²⁻ primary ion beam was accelerated at 13 kV, with an intensity of *c.* 8 nA. The ion beam diameter is about 20 μm \times 30 μm in size. Analysis of the standard zircon Plešovice (337 Ma; Sláma *et al.*, 2008) was interspersed with analysis of unknowns. Each measurement consisted of seven cycles. Pb/U calibration was performed relative to zircon standard Plešovice and U, Th concentrations were calibrated against zircon standard 91500 (Wiedenbeck *et al.*, 1995). An in-house zircon standard Qinghu (159.5 \pm 0.2 Ma; Li *et al.*, 2013b) was alternately analyzed as an unknown together with other unknown zircons to monitor the external uncertainties of SIMS U–Pb zircon dating calibrated against the Plešovice standard. The measurements on the Qinghu zircon yielded concordia ages of 161.1 \pm 1.3 Ma. The instrument description and analytical procedure has been given by Li *et al.* (2013a). Corrections are sufficiently small to be insensitive to the choice of common Pb composition, and an average of present-day crustal composition (Stacey & Kramers, 1975) was used for the common Pb assuming that the common Pb is largely surface contamination introduced during sample preparation. Data reduction was carried out using the Isoplot/Ex v. 3.0 program (Ludwig, 2003). Uncertainties on individual analyses in the data tables are reported at 1 σ level; concordia U–Pb ages are quoted with 95% confidence interval.

Measurements of U–Th–Pb isotopes in zircons for other samples were carried out on an Agilent-7500a quadrupole ICP-MS system coupled with a New Wave SS UP193 laser sampler (LA-ICP-MS) at CUGB. Analytical details were comprehensively described by Song *et al.* (2010). A laser spot size of 36 μm , laser energy density of 8.5 J cm⁻² and a repetition rate of 10 Hz were applied for analysis. The procedure of laser sampling is 5 s pre-ablation, 20 s sample-chamber flushing and 40 s sampling ablation. The ablated material is carried into the ICP-MS system by a high-purity helium gas stream with a flux of 0.8 l min⁻¹. The whole laser path was fluxed with N₂ (15 l min⁻¹) and Ar (1.15 l min⁻¹) to increase energy stability. National Institute of Standards and Technology 610 glass and zircon standard 91500

(Wiedenbeck *et al.*, 1995) were used as external standards, Si as internal standard, and zircon standard Qinghu zircon as the secondary standard. The software GLITTER (ver. 4.4, Macquarie University) was used to process the isotopic ratios and element concentrations in zircons. The common lead correction was made following Andersen (2002). Age calculations and plots of concordia diagrams were made using the Isoplot/Ex v. 3.0 program (Ludwig, 2003).

Zircon Hf–O isotope analysis

In situ zircon Hf isotope analyses were performed on the zircons previously used for LA-ICP-MS U–Pb dating using a Geolas Pro laser ablation system coupled to a Neptune MC-ICP-MS system at the Key Laboratory for the study of focused Magmatism and Giant Ore Deposits, MLR, in the Xi'an Center of the Geological Survey of China. Details of the instrumental conditions and data acquisition procedures are similar to those described by Iizuka & Hirata (2005), Wu *et al.* (2006) and Hou *et al.* (2007). A stationary laser ablation spot with a beam diameter of 44 μm was used for the analyses and the ablation time was 26 s. The ablated aerosol was carried by helium and then combined with argon in a mixing chamber before being introduced to the ICP-MS plasma. Before the analysis, standard zircons (TEMORA, GJ1 and FM02) were analyzed and the isotopes ¹⁷²Yb, ¹⁷³Yb and ¹⁷⁵Lu were simultaneously monitored during each analysis to correct for the interferences of ¹⁷⁶Lu and ¹⁷⁶Yb on ¹⁷⁶Hf. Corrections for ¹⁷⁶Lu and ¹⁷⁶Yb isobaric interferences on readings for ¹⁷⁶Hf used the values of ¹⁷⁶Lu/¹⁷⁵Lu = 0.02658 and ¹⁷⁶Yb/¹⁷³Yb = 0.796218, respectively (Chu *et al.*, 2002). Instrumental mass bias was corrected for by normalizing Hf isotope ratios to ¹⁷⁹Hf/¹⁷⁷Hf = 0.7325 and Yb isotope ratios to ¹⁷²Yb/¹⁷³Yb = 1.35274 (Chu *et al.*, 2002), using the exponential mass fractionation law. Zircon GJ-1 was used as the reference standard and yielded a weighted mean ¹⁷⁶Hf/¹⁷⁷Hf ratio of 0.282030 \pm 40 (2 σ , *n* = 30) during this study, identical to the reference values within analytical error (Morel *et al.*, 2008). A decay constant for ¹⁷⁶Lu of 1.865 \times 10⁻¹¹ a⁻¹ (Scherer *et al.*, 2001) and the present-day chondritic ratios of ¹⁷⁶Hf/¹⁷⁷Hf = 0.282772 and ¹⁷⁶Lu/¹⁷⁷Hf = 0.0332 (Blichert-Toft & Albarède, 1997) were used for calculating $\epsilon_{\text{Hf}}(t)$ values. Depleted mantle model ages (T_{DM1}) were calculated using the measured ¹⁷⁶Lu/¹⁷⁷Hf and ¹⁷⁶Hf/¹⁷⁷Hf ratios with reference to depleted mantle with present-day values of ¹⁷⁶Hf/¹⁷⁷Hf = 0.28325 and ¹⁷⁶Lu/¹⁷⁷Hf = 0.0384 (Griffin *et al.*, 2000). The initial ¹⁷⁶Hf/¹⁷⁷Hf ratios of the zircon were used to calculate the average continental crust model ages (T_{DM2}) assuming a mean crustal ¹⁷⁶Lu/¹⁷⁷Hf value of 0.015 (Griffin *et al.*, 2004). *In situ* zircon O isotope analyses were conducted using a Cameca IMS-1280 SIMS system at the State Key Laboratory of Lithospheric Evolution, Institute of Geology and Geophysics, Chinese Academy of Sciences, Beijing. The zircon O isotope analyses were

conducted prior to the SIMS U–Pb dating to avoid the influence of oxygen implanted in the zircon surface from the O^{2-} beam used for the U–Pb determination. Details of the instrumentation and operating conditions have been given by Li *et al.* (2010a, 2010b). The Cs+ primary ion beam was accelerated at 10 kV, with an intensity of c. 2 nA (Gaussian mode with a primary beam aperture of 200 μm to reduce aberrations) and rastered over a 10 μm area. The analysis spot was about 20 μm in diameter. Oxygen isotopes were measured using multi-collection mode on two off-axis Faraday cups (FC). A nuclear magnetic resonance probe was used for magnetic field control with stability better than 2.5 ppm over 16 h on mass 17. One analysis took \sim 4 min, including pre-sputtering (\sim 120 s), automatic beam centering (\sim 60 s) and integration of oxygen isotopes ($4\text{ s} \times 10$ cycles, total 40 s). With low noise on the two FC amplifiers, the internal precision of a single analysis was generally better than $\pm 0.2\text{‰}$ for $\delta^{18}\text{O}$ values. Measured $^{18}\text{O}/^{16}\text{O}$ was normalized using the Vienna Standard Mean Ocean Water (VSMOW) composition and reported in standard per mil notation with 2σ errors, and then corrected for the instrumental mass fractionation factor (IMF) following the methods of Li *et al.* (2010a). The IMF was corrected using the in-house zircon standard Penglai with a recommended $^{18}\text{O}/^{16}\text{O}$ ratio of 0.0020052 and $(\delta^{18}\text{O})_{\text{VSMOW}}$ value of $5.31 \pm 0.10\text{‰}$ (Li *et al.*, 2010b). Twenty-nine measurements of Penglai yielded a weighted mean $\delta^{18}\text{O} = 5.27 \pm 0.12\text{‰}$ (2σ SD, $n=29$), which agrees well with the recommended $(\delta^{18}\text{O})_{\text{VSMOW}}$ value within error (Li *et al.*, 2010b). During the course of this study, the secondary in-house zircon standard Qinghu was also measured as an unknown to monitor the external precision. Ten measurements of Qinghu yielded a weighted mean $\delta^{18}\text{O} = 5.52 \pm 0.15\text{‰}$ (2σ SD, $n=10$), consistent with the recommended $(\delta^{18}\text{O})_{\text{VSMOW}}$ value of 5.4 ± 0.2 within errors (Li *et al.*, 2013b).

RESULTS

Rock classification

Thin sections of samples were carefully examined under the microscope and most of them had experienced, to different degrees, low-grade metamorphism (e.g. zeolite or prehnite–pumpellyite facies) (Fig. 2e–i). Bulk-rock major and trace element analyses are listed in Table 1 and plotted in Figs 3 and 4. All major element contents were normalized to 100% on a volatile-free basis before plotting. In particular, a small number of samples with high LOI values (Table 1) show different degrees of alteration and thus were removed from the dataset before plotting. Most of the samples fall in the sub-alkaline field, with a few samples lying in the transition field between alkaline and sub-alkaline series on a total alkalis–silica (TAS) diagram (Fig. 3a) and all the samples plot in the sub-alkaline field on a SiO_2 –Zr/TiO₂ diagram (Fig. 3b); this can be attributed to a slight influence on the mobile elements (e.g. Na and K) by the low-

grade metamorphism or alteration. In addition, samples mainly plot in the island arc field on a Hf–Th–Ta diagram (Fig. 3d) and show a calc-alkaline trend on an AFM diagram (Fig. 3c). Accordingly, the lavas can be identified geochemically as (1) boninite, (2) ankaramite, (3) high-Mg basaltic andesite, (4) high-Al andesite and (5) sanukite.

Boninite

The boninites are extensively altered with the development of the typical mineral assemblage of low-grade greenschist-facies conditions (Fig. 2e). Phenocrysts of pyroxene and/or olivine have been altered to pseudomorphs of chlorite, serpentine or tremolite in a groundmass of devitrified glass composed of altered minerals (e.g. chlorite, sericite) and chrome spinel (Fig. 2e). The boninite samples, with moderate SiO_2 (49.7–58.9 wt %), are characterized by variably high contents of MgO (5.0–19.3 wt %), Cr (51–2486 ppm) and Ni (47–453 ppm), but low TiO_2 (mostly <0.5 wt %), and Zr (<55 ppm) contents. In chondrite-normalized REE patterns (Fig. 4a), all boninite samples display variably low REE abundances (4.1 – $17.8 \times \text{C1}$), and have slightly LREE-depleted to LREE-enriched patterns with $(\text{La}/\text{Sm})_{\text{N}}$ ratios of 0.49–1.49, and no to minor negative Eu anomaly ($\text{Eu}/\text{Eu}^* = 0.43$ – 1.07 , with an average of 0.87). In normalized multi-element patterns (Fig. 4b), they are depleted in high field strength elements (HFSE; Nb, Ta, Zr, Hf, P and Ti) and enriched in water-soluble elements (Rb, Ba, U, Pb and Sr).

Ankaramite

The ankaramites are porphyritic with abundant, euhedral Ca-rich Cpx phenocrysts in a usually intersertal to intergranular groundmass filled with plagioclase laths, chloritized glass, or diopside microlites, Fe–Ti oxides, and chrome spinel (Fig. 2f). Chromian spinel grains are visible in the matrix and as inclusions in Cpx grains. The ankaramite samples are characterized by lower SiO_2 contents (48.0–49.2 wt %), but higher contents of MgO (15.0–15.6 wt %), Cr and Ni, relative to the boninites. In chondrite-normalized REE patterns (Fig. 4c), all samples display low REE abundances, slight LREE enrichment with $(\text{La}/\text{Sm})_{\text{N}}$ ratios of 2.70–3.09, and no Eu anomaly. In normalized multi-element patterns (Fig. 4d), the samples are depleted in Nb, Ta, P and Ti and enriched in water-soluble elements (Rb, Ba, U, Pb and Sr).

High-Mg basaltic andesite

The high-Mg basaltic andesites are also porphyritic, with euhedral Ca-rich Cpx and amphibole phenocrysts in a usually intersertal to intergranular groundmass filled with plagioclase laths (Fig. 2g). They have variable SiO_2 (49.6–55.6 wt %) and are characterized by low Al_2O_3 (11.7–17.5 wt %) contents but high MgO (6.7–10.0 wt %), $\text{Fe}_2\text{O}_{3\text{T}}$ (5.6–10.5 wt %), CaO (7.7–12.5 wt %), TiO_2 (0.60–1.21 wt %), Cr (253–503 ppm) and Ni (72–

Table 1: Major and trace element data for Lajishan–Yongjing arc volcanic rocks

Sample: Rock type: Location:	16LJ-10 Boninite XX	16LJ-16 Boninite XX	16LJ-18 Boninite XX	16LJ-26 Boninite XX	12LJ-07 Boninite ZB	12LJ-09 Boninite ZB	LJ15-09 Boninite LK	LJ15-12 Boninite LK	LJ15-13 Boninite LK	LJ15-14 Boninite LK	LJ15-15 Boninite LK	LJ15-108 Boninite YCT	16LJ-07 Boninite XX	16LJ-08 Boninite XX
<i>Major element (wt %)</i>														
SiO ₂	51.56	50.96	50.59	52.33	51.94	49.71	51.52	50.94	57.37	54.80	54.15	55.84	56.11	52.03
TiO ₂	0.09	0.12	0.11	0.08	0.32	0.35	0.36	0.32	0.21	0.69	0.40	0.27	0.25	0.10
Al ₂ O ₃	5.89	7.10	6.22	5.67	11.93	12.49	11.73	13.07	11.68	15.18	10.36	12.23	10.45	6.85
Fe ₂ O _{3t}	9.87	10.40	10.51	10.08	8.75	9.84	8.00	11.51	7.91	9.23	10.04	9.93	9.56	10.93
MnO	0.18	0.19	0.20	0.19	0.14	0.16	0.15	0.18	0.15	0.15	0.17	0.15	0.15	0.15
MgO	16.84	17.12	17.74	17.48	12.67	13.37	12.79	12.50	9.57	7.81	5.91	10.70	11.93	19.31
CaO	11.91	10.25	11.46	10.67	7.15	7.48	8.75	4.92	5.12	4.85	7.83	3.78	5.32	5.17
Na ₂ O	1.19	1.32	0.93	1.35	2.31	1.32	2.04	2.83	4.06	4.62	3.67	3.62	3.19	0.56
K ₂ O	0.23	0.14	0.29	0.25	0.90	1.16	2.39	0.70	0.19	0.04	0.12	0.31	0.11	0.04
P ₂ O ₅	0.02	0.02	0.02	0.03	0.03	0.04	0.03	0.06	0.03	0.06	0.14	0.04	0.03	0.03
LOI	1.30	1.52	1.64	1.44	3.12	3.44	2.56	3.13	3.30	2.49	6.85	2.81	1.79	3.73
Total	99.1	99.1	99.7	99.6	99.3	99.4	100.3	100.2	99.6	99.9	99.6	99.7	98.9	98.9
Mg#	79.9	79.3	79.7	80.2	77.1	76.0	78.8	71.7	73.8	66.3	57.8	71.5	74.4	80.5
<i>Trace element (ppm)</i>														
Sc	25.9	31.8	24.7	22.6	43.3	49.1	35.5	47.6	41.9	50.5	39.0	40.3	30.8	26.7
Ti	586.2	953.2	673.2	502.6	2140	2348	2268	2136	1417	4930	2662	1883	1701	691.8
V	116.2	141.0	95.5	92.3	221.0	239.6	202.8	316.8	174.3	316.8	165.7	239.2	172.8	133.3
Cr	2150.0	2270.0	2282.0	1839.0	721.6	934.8	903.8	608.2	556.8	259.8	1702.6	833.2	653.0	1806.0
Co	59.1	70.0	64.0	67.3	40.2	46.6	49.2	54.5	43.8	46.7	78.3	53.7	46.1	71.4
Ni	420.6	408.0	423.6	333.0	193.9	234.4	265.2	152.3	114.2	87.8	445.6	210.2	140.4	453.6
Cu	5.5	12.6	2.0	33.5	135.8	144.7	82.0	56.6	86.6	116.3	1.7	70.2	119.8	19.8
Zn	61.2	65.3	63.2	59.5	52.3	63.6	88.0	93.5	65.5	76.1	65.6	80.5	50.1	68.5
Ga	6.3	8.5	6.8	5.5	8.8	10.5	9.8	14.7	10.5	14.0	7.2	12.9	11.0	8.3
Rb	3.1	2.4	5.1	3.3	41.3	55.5	95.4	17.6	3.1	0.4	3.4	4.0	2.0	0.3
Sr	120.1	122.8	48.8	115.1	85.9	122.0	152.5	171.4	140.4	261.2	211.0	152.0	169.2	25.2
Y	3.5	4.5	3.2	2.7	9.6	9.6	10.4	10.6	6.4	22.2	25.8	8.4	7.8	4.1
Zr	18.1	25.8	17.8	16.4	18.0	22.6	24.4	50.5	28.7	52.4	26.8	36.0	38.0	30.0
Nb	0.6	0.8	0.6	0.5	1.3	1.5	2.0	1.2	1.0	0.6	0.4	0.8	1.4	1.1
Cs	0.1	0.2	0.2	0.1	1.7	2.3	1.6	0.8	0.4	0.1	0.3	0.3	0.1	0.3
Ba	43.6	27.8	67.0	65.2	59.6	54.9	390.0	174.8	54.5	36.2	19.7	59.5	27.9	8.6
Ce	1.3	1.5	1.0	1.0	2.1	2.9	1.0	3.5	2.2	1.8	2.0	2.6	2.2	1.6
Pr	3.4	4.1	2.9	2.5	4.8	6.3	3.0	10.0	5.4	6.3	3.3	6.7	5.7	4.8
Nd	0.5	0.6	0.4	0.3	0.6	0.8	0.5	1.5	0.7	1.2	0.9	0.9	0.8	0.7
Sm	2.1	2.6	1.7	1.6	2.9	3.6	2.6	6.8	3.2	6.4	4.9	4.3	3.6	3.1
Eu	0.5	0.7	0.5	0.4	0.9	0.4	1.0	0.7	0.3	0.9	0.7	0.4	0.4	0.2
Gd	0.2	0.2	0.2	0.2	0.3	0.4	0.4	0.7	0.3	0.9	0.7	0.4	0.4	0.2
Tb	0.6	0.8	0.5	0.5	1.2	1.3	1.5	2.2	1.2	3.5	2.7	1.6	1.2	0.8
Dy	0.1	0.1	0.1	0.1	0.2	0.2	0.3	0.4	0.2	0.7	0.5	0.3	0.2	0.1
Ho	0.1	0.2	0.1	0.1	0.4	0.4	0.5	0.5	0.3	1.1	1.0	0.4	0.3	0.2
Er	0.4	0.5	0.3	0.3	1.1	1.1	1.4	1.4	0.9	3.0	3.0	1.1	0.8	0.4
Tm	0.1	0.1	0.0	0.0	0.2	0.2	0.2	0.2	0.1	0.5	0.4	0.2	0.1	0.1
Yb	0.4	0.5	0.3	0.3	1.2	1.2	1.4	1.4	0.9	3.0	2.9	1.2	0.9	0.4
Lu	0.1	0.1	0.1	0.0	0.2	0.2	0.2	0.2	0.1	0.5	0.5	0.2	0.1	0.1
Hf	0.4	0.6	0.4	0.4	0.4	0.6	0.8	1.5	0.9	1.6	0.8	1.1	0.9	0.7
Ta	0.0	0.1	0.1	0.0	0.1	0.1	0.2	0.1	0.1	0.0	0.0	0.1	0.1	0.1
Pb	0.8	0.8	0.7	0.6	1.2	1.8	2.1	2.5	5.7	2.8	4.8	3.4	1.8	0.3
Th	0.2	0.3	0.2	0.1	0.3	0.3	0.4	0.1	0.1	0.4	0.4	0.1	0.4	0.3
U	0.3	0.2	0.2	0.2	0.1	0.1	0.3	0.5	0.3	0.1	0.1	0.3	0.3	0.3

(continued)

Table 1: Continued

Sample no.:	16LJ-09	16LJ-15	16LJ-47	16LJ-48	16LJ-56	16LJ-57	16LJ-58	16LJ-59	16LJ-61	16LJ-62	16LJ-63	LJ15-106
Rock type:	Boninite											
Location:	XX	XX	ZB	YCT								
<i>Major element (wt%)</i>												
SiO ₂	58.93	53.99	51.38	54.39	56.20	56.59	57.96	58.82	57.20	54.03	53.21	57.73
TiO ₂	0.21	0.16	0.28	0.52	0.13	0.14	0.14	0.13	0.27	0.29	0.31	0.40
Al ₂ O ₃	8.21	7.59	11.31	13.69	8.43	8.28	8.24	7.92	9.88	11.65	11.37	14.02
Fe ₂ O _{3t}	9.66	9.93	10.23	10.32	10.65	11.09	10.97	10.83	8.76	9.04	9.09	8.84
MnO	0.14	0.14	0.15	0.17	0.17	0.18	0.17	0.17	0.11	0.10	0.11	0.12
MgO	11.68	16.59	10.75	8.65	8.16	9.29	9.46	9.41	11.32	11.03	12.38	5.80
CaO	5.76	5.84	6.08	5.29	6.99	6.40	5.58	5.43	6.79	8.21	8.14	4.19
Na ₂ O	2.32	2.25	1.50	4.63	1.23	1.26	1.25	1.19	2.45	2.87	2.57	3.17
K ₂ O	0.09	0.12	0.35	0.23	0.03	0.04	0.03	0.04	0.34	0.51	0.50	0.09
P ₂ O ₅	0.04	0.04	0.02	0.06	0.02	0.02	0.03	0.02	0.04	0.04	0.04	0.05
LOI	2.22	1.56	7.68	1.76	7.30	5.99	5.40	5.21	2.32	1.98	2.06	5.15
Total	98.6	98.9	99.7	99.7	99.3	99.3	99.2	99.2	99.5	99.8	99.8	99.5
Mg#	73.8	79.6	71.0	66.1	64.1	66.1	66.8	66.9	75.1	74.0	76.0	60.4
<i>Trace element (ppm)</i>												
Sc	28.6	36.4	47.0	42.5	27.6	27.6	30.0	29.0	41.3	35.0	37.7	46.8
Ti	1555	1349	1955	3358	836.2	924.4	916.2	893.2	2150	1848	2074	2866
V	185.6	149.6	255.8	261.6	129.9	139.5	143.3	142.0	243.8	231.0	228.4	321.4
Cr	699.2	2486.0	691.0	757.4	966.6	960.8	876.0	1012.8	887.6	640.0	763.6	159.5
Co	41.3	71.4	40.7	52.5	42.7	45.4	45.7	47.7	40.3	33.5	34.1	36.7
Ni	140.4	449.8	125.7	196.4	109.4	109.8	99.1	115.2	189.3	140.6	179.2	56.9
Cu	126.0	1.7	46.8	43.9	1.8	1.5	8.5	6.4	22.7	9.8	8.8	32.3
Zn	83.4	72.1	64.1	65.1	73.2	78.9	74.9	85.0	33.5	27.2	32.1	71.4
Ga	9.5	10.1	10.2	12.7	10.5	10.5	9.8	10.1	9.2	8.9	8.7	14.3
Rb	1.8	1.6	6.5	3.2	0.6	0.7	0.8	0.8	20.5	19.4	26.2	1.3
Sr	131.4	186.5	78.3	77.4	45.0	36.3	30.6	30.9	123.3	112.8	129.9	123.3
Y	7.9	6.4	7.7	13.2	9.6	9.2	5.4	6.6	11.1	9.4	10.3	12.1
Zr	32.4	33.3	11.7	39.4	28.5	31.5	31.4	29.2	16.8	14.1	16.3	39.7
Nb	1.2	1.1	0.4	0.5	0.9	1.0	1.1	1.0	1.3	1.1	1.3	0.7
Cs	0.4	0.4	0.5	0.0	0.3	0.2	0.2	0.2	0.8	0.5	1.0	0.0
Ba	21.9	33.5	37.7	44.3	4.8	5.1	6.7	6.5	41.7	49.4	39.6	28.4
La	1.9	2.3	1.1	2.5	1.4	1.2	1.2	1.2	1.9	1.6	1.7	3.5
Ce	5.6	6.1	2.7	7.2	4.0	3.8	3.7	3.6	4.8	4.0	4.4	9.5
Pr	0.8	0.8	0.4	1.1	0.6	0.6	0.6	0.6	0.7	0.6	0.6	1.4
Nd	3.6	3.8	1.7	5.7	3.1	3.0	2.6	2.8	3.1	2.6	2.9	6.6
Sm	1.0	1.0	0.6	1.8	1.0	1.0	0.9	0.8	0.8	0.8	0.8	2.0
Eu	0.3	0.3	0.1	0.6	0.3	0.3	0.2	0.2	0.3	0.3	0.3	0.7
Gd	1.2	1.1	0.9	2.1	1.3	1.3	0.8	1.0	1.2	1.1	1.2	2.3
Tb	0.2	0.2	0.2	0.4	0.2	0.2	0.1	0.2	0.2	0.2	0.2	0.4
Dy	1.3	1.2	1.3	2.3	1.3	1.4	0.9	1.0	1.7	1.4	1.5	2.6
Ho	0.3	0.3	0.3	0.5	0.3	0.3	0.2	0.2	0.4	0.3	0.4	0.6
Er	0.8	0.7	0.9	1.5	0.8	0.9	0.5	0.6	1.2	1.0	1.1	1.7
Tm	0.1	0.1	0.1	0.2	0.1	0.1	0.1	0.1	0.2	0.2	0.2	0.3
Yb	0.9	0.7	1.0	1.4	0.8	0.9	0.5	0.6	1.3	1.1	1.2	1.7
Lu	0.1	0.1	0.2	0.2	0.1	0.1	0.1	0.1	0.2	0.2	0.2	0.3
Hf	0.8	0.8	0.4	1.0	0.7	0.8	0.7	0.7	0.4	0.4	0.4	1.3
Ta	0.1	0.1	0.0	0.0	0.1	0.1	0.1	0.1	0.1	0.1	0.1	0.1
Pb	1.8	1.6	4.2	2.9	0.5	0.4	0.6	0.6	1.0	0.7	0.9	2.2
Th	0.4	0.4	0.3	0.4	0.7	0.7	0.7	0.6	0.3	0.3	0.3	0.2
U	0.3	0.3	0.1	0.2	0.2	0.2	0.2	0.2	0.0	0.0	0.1	0.2

(continued)

Table 1: Continued

Sample:	13QLS-68	13QLS-70	13QLS-71	13QLS-72	13QLS-121	13QLS-124	13QLS-134	LJ15-20	LJ15-38	LJ15-39	LJ15-40	LJ15-42
Rock type:	Ank	Ank	Ank	Ank	HMBA	HMBA	HMBA	HMBA	HMBA	HMBA	HMBA	HMBA
Location:	XX	XX	XX	XX	YJ	YJ	YJ	ZB	ZB	ZB	ZB	ZB
<i>Major element (wt %)</i>												
SiO ₂	48.75	48.63	48.00	49.18	53.81	52.45	51.75	55.60	54.63	49.91	55.62	55.28
TiO ₂	0.74	0.74	0.77	0.76	0.94	0.99	1.01	0.95	0.78	1.21	0.81	0.81
Al ₂ O ₃	11.48	10.36	10.70	10.96	13.71	13.99	13.11	15.91	14.56	17.46	14.68	15.26
Fe ₂ O _{3t}	10.19	9.35	10.13	10.27	8.93	9.20	9.21	6.82	5.62	7.44	5.82	6.21
MnO	0.18	0.20	0.19	0.18	0.22	0.36	0.19	0.13	0.11	0.11	0.10	0.11
MgO	15.05	15.34	15.62	14.95	8.05	8.56	7.37	7.27	6.66	7.25	7.36	8.31
CaO	8.99	9.99	9.63	9.21	6.37	7.62	8.44	4.73	6.70	8.19	5.75	5.42
Na ₂ O	1.94	2.06	2.19	1.82	2.74	2.04	2.43	2.47	5.00	3.82	3.69	2.94
K ₂ O	0.82	0.86	0.39	0.72	1.34	0.95	2.81	2.36	0.46	1.19	2.18	2.12
P ₂ O ₅	0.39	0.40	0.43	0.40	0.32	0.30	0.27	0.20	0.19	0.40	0.20	0.20
LOI	1.69	2.51	2.46	2.25	2.84	2.57	2.41	3.51	5.20	3.55	3.66	3.33
Total	100.2	100.4	100.5	100.6	99.3	99.0	99.0	99.9	99.9	100.5	99.9	100.0
Mg#	77.02	77.02	78.23	77.23	67.8	68.5	65.1	71.3	73.4	69.4	74.7	75.7
<i>Trace element (ppm)</i>												
Sc	37.4	37.5	41.7	38.9	40.4	49.8	43.9	28.4	26.7	24.1	26.5	27.2
Ti	4466	4632	4998	4780	5635	5932	6080.1	7000	5626	7644	5870	5562
V	2068	203.0	223.4	211.4	245.2	341.2	299.4	190.7	158.8	154.9	170.2	166.0
Cr	1294.8	1126.2	1341.0	1270.2	419.4	501.4	481.6	253.2	442.8	339.8	435.0	449.8
Co	52.5	50.0	55.6	56.3	61.6	46.3	42.1	38.9	35.9	38.1	37.9	38.7
Ni	340.4	312.0	377.4	352.0	77.9	72.8	114.2	106.9	195.7	186.6	198.5	195.8
Cu	53.5	56.8	79.0	66.8	35.5	186.8	59.0	46.0	67.1	67.3	56.3	40.3
Zn	65.3	61.0	66.5	67.6	129.8	87.1	76.1	181.6	110.9	60.2	60.0	60.8
Ga	13.2	12.1	14.1	14.1	15.8	18.0	17.2	18.5	17.8	20.5	17.0	16.4
Rb	15.2	12.3	7.6	14.1	49.8	26.4	47.8	121.5	8.8	15.9	33.5	46.2
Sr	225.8	221.4	150.8	289.0	270.2	307.0	350.8	386.4	253.6	867.2	370.8	399.0
Y	14.7	15.4	16.4	15.9	20.5	21.1	22.3	22.1	16.3	21.3	17.8	16.5
Zr	76.6	81.8	86.6	81.8	90.3	87.2	94.1	148.3	116.1	181.6	121.2	116.1
Nb	12.4	13.0	13.5	12.8	11.9	12.4	12.0	12.4	14.5	30.9	15.3	14.4
Cs	1.5	1.2	1.0	1.7	2.3	1.5	0.4	3.1	0.7	1.8	1.2	1.6
Ba	351.0	464.6	198.7	326.8	431.8	289.4	643.2	1219.6	123.8	452.6	842.8	636.4
La	17.0	18.9	17.7	18.5	17.0	15.8	14.6	28.5	27.0	41.6	28.5	27.3
Ce	37.5	41.4	40.4	41.0	34.7	34.5	30.2	58.5	51.0	81.6	54.7	52.0
Pr	4.5	5.0	5.0	5.0	4.1	4.1	3.7	7.2	5.8	9.8	6.2	5.9
Nd	17.4	18.9	19.6	19.1	16.8	16.7	15.3	26.4	21.0	35.9	22.2	21.4
Sm	3.7	4.0	4.2	4.0	3.9	3.8	3.7	5.3	4.1	6.5	4.4	4.2
Eu	1.2	1.2	1.3	1.3	1.2	1.2	1.2	1.6	1.4	2.1	1.6	1.4
Gd	3.5	3.7	4.0	3.8	4.0	3.7	3.8	5.0	3.9	5.7	4.2	4.0
Tb	0.5	0.5	0.6	0.6	0.6	0.6	0.6	0.8	0.6	0.8	0.6	0.6
Dy	2.9	3.0	3.3	3.2	3.8	3.5	3.6	4.4	3.4	4.4	3.6	3.4
Ho	0.6	0.6	0.7	0.6	0.8	0.7	0.7	0.9	0.7	0.9	0.8	0.7
Er	1.6	1.6	1.7	1.7	2.2	2.1	2.1	2.5	2.0	2.5	2.1	2.0
Tm	0.2	0.2	0.2	0.2	0.3	0.3	0.3	0.4	0.3	0.4	0.3	0.3
Yb	1.4	1.4	1.5	1.5	2.0	1.8	1.9	2.2	1.8	2.3	1.9	1.8
Lu	0.2	0.2	0.2	0.2	0.3	0.3	0.3	0.3	0.3	0.4	0.3	0.3
Hf	1.7	1.9	2.0	1.9	2.2	2.2	2.4	3.5	2.7	3.7	2.9	2.8
Ta	0.8	0.8	0.8	0.8	0.7	0.7	0.7	0.8	1.1	1.7	1.0	0.9
Pb	2.8	3.9	4.6	4.2	3.6	6.5	8.5	9.2	14.9	21.0	19.3	14.5
Th	2.4	2.6	2.7	2.6	4.6	4.3	3.1	8.1	6.6	8.0	7.1	6.6
U	0.8	0.8	0.9	0.8	0.7	0.8	0.7	2.3	2.3	2.4	2.4	2.2

(continued)

Table 1: Continued

Sample:	LJ15-166	LJ15-167	16LJ-27	16LJ-32	13QLS16	13QLS17	13QLS58	13QLS61	13QLS86	13QLS89	13QLS92	13QLS95	13QLS100
Rock type:	HMBA	HMBA	HMBA	HMBA	HAA								
Location:	YJ	YJ	XX	CP	MC	MC	XX	XX	CP	CP	CP	CP	YJ
<i>Major element (wt%)</i>													
SiO ₂	51.24	53.11	54.63	49.61	49.10	54.52	51.49	55.56	60.19	60.55	52.81	48.65	54.76
TiO ₂	1.03	0.93	0.62	0.60	0.76	0.78	0.92	0.83	0.82	0.53	0.84	0.74	0.57
Al ₂ O ₃	15.94	12.91	14.26	11.74	18.72	17.90	19.17	16.38	18.00	18.70	18.78	23.06	20.82
Fe ₂ O _{3t}	9.55	9.57	7.69	10.51	9.71	9.15	8.46	8.57	6.92	4.98	8.28	8.73	7.11
MnO	0.33	0.19	0.14	0.17	0.16	0.14	0.14	0.14	0.11	0.09	0.09	0.17	0.13
MgO	8.40	8.80	7.53	9.86	5.48	3.63	4.63	2.86	2.19	1.14	1.63	3.92	2.97
CaO	7.35	10.47	7.73	12.52	6.52	3.94	8.79	6.12	2.26	2.83	9.79	4.36	6.75
Na ₂ O	3.04	1.62	4.16	1.27	5.07	6.59	3.41	5.44	6.84	4.78	5.99	7.40	3.85
K ₂ O	0.70	0.61	0.77	0.93	0.86	0.37	0.86	1.48	0.36	1.69	0.01	0.28	0.99
P ₂ O ₅	0.33	0.28	0.13	0.14	0.20	0.21	0.17	0.19	0.36	0.17	0.26	0.15	0.23
LOI	2.45	1.76	1.63	2.19	2.91	2.22	0.96	2.01	1.61	3.36	1.79	2.59	1.92
Total	100.4	100.3	99.3	99.5	99.5	99.4	99.0	99.6	99.4	98.8	100.3	100.1	100.1
Mg#	67.2	68.2	69.5	68.6	56.8	48.1	56.0	43.8	42.4	34.7	31.5	51.2	49.3
<i>Trace element (ppm)</i>													
Sc	44.7	44.8	26.8	52.0	35.1	32.8	39.4	17.4	15.1	11.3	21.4	25.2	16.5
Ti	6839	6414	3664	3486	4884	5102	5494	5279	5360	3570	5624	4902	3802
V	266.5	291.4	197.9	295.6	266.2	259.6	312.6	202.3	100.2	11.1	154.0	248.0	134.6
Cr	449.9	503.4	310.2	434.8	108.3	99.9	63.9	26.5	5.1	4.4	25.0	19.9	58.5
Co	50.5	41.5	32.6	48.3	25.6	24.5	31.5	20.6	10.9	4.9	21.4	27.5	17.4
Ni	76.5	72.1	87.6	87.1	38.4	35.5	22.5	14.9	3.6	2.8	18.7	12.9	24.6
Cu	27.9	145.5	6.7	66.5	72.3	74.8	46.3	9.4	10.7	19.2	14.4	14.1	28.0
Zn	90.8	82.4	64.4	57.7	77.0	76.6	74.3	63.8	63.1	46.2	51.2	76.7	66.3
Ga	17.7	17.3	14.8	11.8	17.9	18.0	19.4	14.8	13.3	17.5	17.7	17.3	18.5
Rb	20.5	17.7	15.3	14.9	8.7	5.0	22.7	28.8	1.5	39.0	0.4	4.3	23.4
Sr	430.8	651.4	458.6	472.6	396.2	398.6	406.2	402.1	145.0	135.3	99.5	390.6	1154.2
Y	21.2	20.1	13.3	14.0	13.8	14.3	21.2	18.7	29.2	42.4	19.0	21.8	15.2
Zr	97.7	90.1	51.5	47.0	91.9	99.5	61.8	78.2	175.7	264.4	82.2	92.3	69.9
Nb	13.7	12.2	4.2	4.3	13.2	14.4	5.6	5.6	24.2	46.2	11.6	6.4	10.6
Cs	1.8	0.6	2.1	1.8	0.7	0.4	2.4	2.7	0.1	1.2	0.0	0.2	1.6
Ba	296.8	269.0	259.0	342.2	326.8	138.2	254.8	288.0	51.1	235.6	26.2	234.6	360.2
La	18.2	18.1	9.3	9.8	13.7	13.0	7.9	7.0	21.8	33.6	10.8	13.0	19.4
Ce	35.8	35.0	20.0	21.4	28.8	27.4	17.9	17.3	47.5	68.5	23.6	27.3	40.2
Pr	4.4	4.2	2.6	2.7	3.3	3.3	2.4	2.2	5.7	8.0	3.0	3.3	4.7
Nd	17.6	16.8	10.4	11.1	12.6	12.3	10.5	9.7	21.9	29.7	12.0	13.3	17.5
Sm	4.1	3.9	2.4	2.8	2.8	2.7	2.8	2.7	5.1	6.7	3.0	3.3	3.6
Eu	1.3	1.3	0.8	0.8	1.0	0.9	1.0	1.0	1.3	1.4	1.0	1.0	1.2
Gd	4.6	4.4	2.4	2.9	2.8	2.7	3.1	3.1	5.4	6.9	3.3	3.6	3.3
Tb	0.8	0.7	0.4	0.4	0.4	0.4	0.5	0.5	0.9	1.2	0.5	0.6	0.5
Dy	4.6	4.4	2.2	2.5	2.5	2.5	3.2	3.3	5.2	7.3	3.3	3.8	2.9
Ho	1.0	1.0	0.5	0.5	0.5	0.5	0.7	0.7	1.1	1.6	0.7	0.8	0.6
Er	2.7	2.6	1.3	1.4	1.5	1.6	1.9	2.1	3.2	4.7	2.0	2.4	1.7
Tm	0.4	0.4	0.2	0.2	0.2	0.2	0.3	0.3	0.5	0.7	0.3	0.4	0.2
Yb	2.5	2.5	1.2	1.2	1.4	1.5	1.8	1.9	3.1	4.9	1.9	2.4	1.6
Lu	0.4	0.4	0.2	0.2	0.2	0.2	0.3	0.3	0.5	0.8	0.3	0.4	0.2
Hf	2.9	2.9	1.2	1.1	2.3	2.5	1.7	1.8	3.9	6.1	2.0	2.4	1.7
Ta	1.1	0.8	0.2	0.2	0.8	0.9	0.3	0.4	1.8	2.8	0.7	0.5	0.7
Pb	7.2	10.5	3.0	3.5	7.1	10.8	1.8	3.9	4.3	6.4	2.3	5.3	13.3
Th	5.3	4.7	1.5	2.6	2.5	2.6	1.2	1.2	5.8	8.7	2.0	3.4	4.0
U	1.6	1.2	0.4	0.6	0.8	0.9	0.3	0.5	1.6	2.1	0.3	1.3	1.1

(continued)

Table 1: Continued

Sample:	13QLS103	13QLS123	LJ15-70	LJ15-109	12LJ-13	12LJ-14	12LJ-15	Lj-3	Lj-4	Lj-5	12LJ-05	LJ15-52	LJ15-53
Rock type:	HAA	HAA	HAA	HAA	Sanukite								
Location:	YJ	YJ	SHN	YCT	ZB								
<i>Major element (wt %)</i>													
SiO ₂	51.14	60.44	54.38	58.14	54.51	55.53	60.73	54.93	56.87	55.70	63.61	64.81	65.83
TiO ₂	0.55	0.78	0.79	0.70	0.76	0.77	0.68	0.71	0.73	0.77	0.52	0.44	0.60
Al ₂ O ₃	19.36	16.17	17.32	18.94	13.53	13.87	12.51	13.10	14.16	14.47	14.41	13.75	15.40
Fe ₂ O _{3t}	7.66	7.06	8.16	7.42	6.66	6.49	5.67	7.08	6.75	7.50	3.44	3.58	4.23
MnO	0.15	0.11	0.11	0.15	0.07	0.06	0.05	0.07	0.05	0.06	0.05	0.05	0.08
MgO	4.03	2.39	2.67	3.50	6.20	6.32	4.67	6.96	5.43	7.23	2.58	2.36	2.88
CaO	6.06	4.54	5.61	6.06	5.26	5.50	5.06	5.23	5.95	7.23	2.81	3.65	2.15
Na ₂ O	3.12	3.01	2.73	7.68	2.42	2.49	2.19	2.83	2.73	3.11	4.96	3.08	3.73
K ₂ O	4.06	1.89	0.91	0.10	1.55	1.64	1.24	1.25	1.28	1.17	1.20	1.04	2.60
P ₂ O ₅	0.24	0.16	0.13	0.39	0.25	0.25	0.22	0.21	0.22	0.22	0.19	0.17	0.20
LOI	3.03	2.22	7.15	1.90	7.94	6.23	5.96	6.97	5.20	5.44	5.09	6.38	2.05
Total	99.4	98.8	99.9	99.6	99.2	99.1	99.0	99.3	99.4	99.3	98.9	99.7	99.7
Mg#	55.1	44.1	43.2	52.4	68.4	69.4	65.8	69.6	65.2	69.2	63.5	60.6	61.4
<i>Trace element (ppm)</i>													
Sc	16.2	20.5	29.9	5.6	22.0	21.6	19.7	22.2	21.4	24.0	11.1	9.8	13.4
Ti	3670	4681	5580	4486	5048	4960	4498	5420	5380	5886	3508	3422	4330
V	145.2	198.3	244.6	10.7	164.0	164.4	145.6	194.0	193.3	207.6	92.1	82.1	115.8
Cr	90.0	105.8	12.9	2.0	444.2	421.6	384.4	500.2	460.8	521.8	88.7	68.6	90.4
Co	20.9	23.4	26.0	6.2	21.1	20.0	16.8	29.3	25.3	22.6	7.0	13.7	11.9
Ni	23.4	34.2	9.7	1.4	135.6	125.9	110.5	138.7	127.0	130.1	16.7	19.1	25.5
Cu	37.1	34.7	69.8	25.7	25.9	210.6	300.0	95.5	461.2	318.6	3.3	15.4	12.5
Zn	60.9	76.5	66.3	125.5	48.6	42.4	33.9	61.5	51.2	52.4	30.6	101.7	119.1
Ga	17.1	20.6	18.7	20.1	18.1	19.1	17.0	18.2	19.3	20.9	19.4	18.3	20.1
Rb	74.1	66.2	21.1	1.1	63.5	86.1	61.0	72.7	74.9	70.6	70.9	50.3	63.7
Sr	569.6	649.8	274.0	250.0	283.2	416.0	264.2	279.6	346.4	274.4	241.2	412.2	498.0
Y	18.0	17.5	19.4	36.4	13.9	16.3	15.1	15.9	14.2	13.8	12.8	10.3	15.2
Zr	108.3	145.8	79.2	278.0	138.1	150.6	135.5	130.0	133.8	134.3	143.0	144.6	161.9
Nb	15.4	14.2	4.7	36.2	22.0	21.9	20.2	21.1	21.0	22.1	21.9	20.8	24.9
Cs	0.6	2.0	1.4	0.3	3.5	2.4	3.9	2.3	3.0	2.9	4.1	3.0	2.1
Ba	748.0	599.4	278.2	142.9	613.4	995.6	255.2	391.8	316.6	334.6	226.6	139.6	1088.6
La	18.6	21.6	6.4	39.6	40.7	37.6	31.6	36.3	27.8	26.5	25.5	32.5	37.8
Ce	36.7	44.7	15.2	80.2	73.4	68.3	59.5	67.8	52.0	50.0	46.5	58.7	68.7
Pr	4.2	5.3	2.2	9.8	7.8	7.5	6.7	7.4	5.7	5.5	5.1	6.2	7.4
Nd	15.3	20.2	9.8	37.0	27.5	27.3	25.0	26.9	21.4	20.0	19.1	20.9	25.7
Sm	3.3	4.0	2.7	7.5	4.5	4.8	4.4	4.6	3.9	3.5	3.5	3.4	4.6
Eu	1.0	1.1	0.7	2.2	1.3	1.4	1.2	1.3	1.2	1.0	1.0	1.0	1.5
Gd	3.3	3.5	3.3	7.5	3.6	4.1	3.8	3.9	3.4	3.1	3.1	2.9	4.0
Tb	0.5	0.5	0.6	1.2	0.5	0.5	0.5	0.5	0.5	0.4	0.4	0.4	0.6
Dy	3.2	2.9	4.0	7.4	2.7	3.1	2.8	3.0	2.6	2.5	2.4	2.2	3.3
Ho	0.7	0.6	0.9	1.7	0.5	0.6	0.5	0.6	0.5	0.5	0.5	0.5	0.7
Er	2.0	1.7	2.7	4.9	1.5	1.7	1.5	1.7	1.4	1.5	1.3	1.3	1.8
Tm	0.3	0.2	0.4	0.8	0.2	0.2	0.2	0.2	0.2	0.2	0.2	0.2	0.3
Yb	1.9	1.5	2.7	5.2	1.4	1.6	1.4	1.5	1.3	1.4	1.2	1.4	1.8
Lu	0.3	0.2	0.4	0.8	0.2	0.2	0.2	0.2	0.2	0.2	0.2	0.2	0.3
Hf	2.7	3.5	2.3	7.0	3.6	3.8	3.5	3.0	3.1	3.1	3.8	4.2	4.6
Ta	1.0	0.8	0.3	2.5	1.4	1.4	1.3	1.3	1.3	1.3	1.5	1.6	2.1
Pb	10.5	15.5	4.9	6.2	3.5	3.5	3.6	2.0	2.8	1.4	4.4	12.7	14.1
Th	4.7	6.9	1.1	7.1	10.1	8.9	8.0	6.6	6.9	7.1	8.0	12.0	14.0
U	1.5	1.2	0.5	1.7	1.8	2.1	2.1	1.9	2.0	2.0	2.0	2.8	3.3

Ank, ankaramite; HMBA, high-Mg basaltic andesite; HAA, high-Al andesite; LK, Lajishankou; XX, Xiongxian; CP, Chapu; ZB, Zhaba; SHN, Sihanning; MC, Machang; YCT, Yaocao tai; YJ, Yongjing.

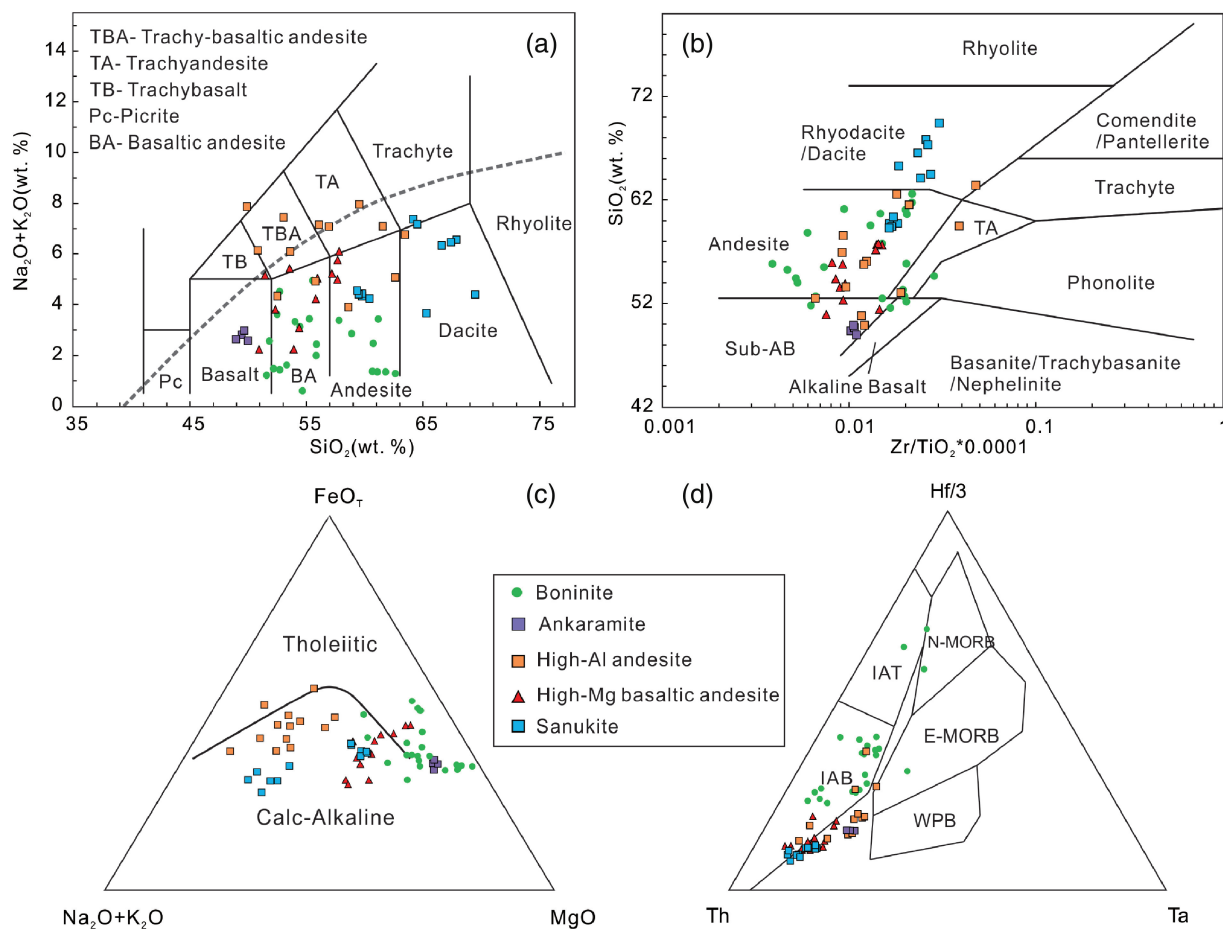


Fig. 3. (a) TAS diagram (Le Maitre, 2002); (b) SiO_2 – Zr/TiO_2 diagram (Winchester & Floyd, 1977) Sub-AB, sub-alkaline basalt, TA, Trachyandesite; (c) AFM diagram (Pearce *et al.*, 1977); (d) Hf–Th–Ta diagram (Wood, 1980). IAB, island arc basalt; IAT, island arc tholeiite; WPB, within-plate basalt.

198 ppm). Their chondrite-normalized REE patterns show LREE enrichment with $(\text{La}/\text{Sm})_N$ ratios of 2.24–4.26 and no Eu anomalies (Fig. 4c). In normalized multi-element patterns (Fig. 4d), they are depleted in HFSE (Nb, Ta, Zr, Hf, P and Ti) and enriched in LILE (Rb, Ba, Pb, Sr and Th).

High-Al andesite

The high-Al andesites have porphyritic textures with abundant euhedral, lath-shaped plagioclase and minor embayed pyroxene and amphibole pseudomorphs in an intersertal groundmass filled with plagioclase laths and glass as well as opaque minerals (Fig. 2h). They are of basaltic andesite to dacite composition with moderate SiO_2 (48.7–60.5 wt %) and a relatively large compositional range in terms of other major elements (Table 1; Fig. 3). In addition, they are characterized by high Al_2O_3 (16.2–23.1 wt %) contents but low MgO (1.1–5.5 wt %), Cr (2.0–108.3 ppm) and Ni (1.4–38.4 ppm). Their chondrite-normalized REE patterns show LREE enrichment with $(\text{La}/\text{Sm})_N$ ratios of 1.69–5.34 and no to negative Eu anomalies ($\text{Eu}/\text{Eu}^* = 0.90$ –1.15) (Fig. 4e). In normalized multi-element patterns, they are depleted in HFSE (Nb, Ta, Zr, Hf and Ti) and enriched in mobile

elements (Rb, Ba, U, Th and Pb) (Fig. 4f). The covariation of negative Sr and Eu anomalies occurs in some samples, and may result from the crystallization of plagioclase.

Sanukite

Sanukites are white in color with a porphyritic texture in the field, and show sulfide mineralization. The phenocryst minerals are mainly plagioclase and quartz with minor pyroxene pseudomorphs (Fig. 2i). The plagioclase phenocrysts are lath-shaped, and the olivine or pyroxene phenocrysts are euhedral and have been altered to chlorite. The matrix is mainly composed of fine-grained plagioclase and glass. Geochemically, they are characterized by andesite to dacite composition with SiO_2 (54.5–60.7 wt %), high K_2O (>1.0 wt %), $\text{Mg}\# > 65$ and high Cr (384–521 ppm) and Ni (111–139 ppm). The evolved equivalent dacite samples ($\text{Mg}\# = 55$ –64) have high SiO_2 (61.6–65.8 wt %) and low Cr (46–113 ppm) and Ni (10–26 ppm) contents. The chondrite-normalized REE patterns show LREE enrichment with $(\text{La}/\text{Sm})_N$ ratios of 4.6–6.2 and no to minor negative Eu anomalies ($\text{Eu}/\text{Eu}^* = 0.76$ –1.04) (Fig. 4g). In normalized multi-element patterns (Fig. 4h), they are variously

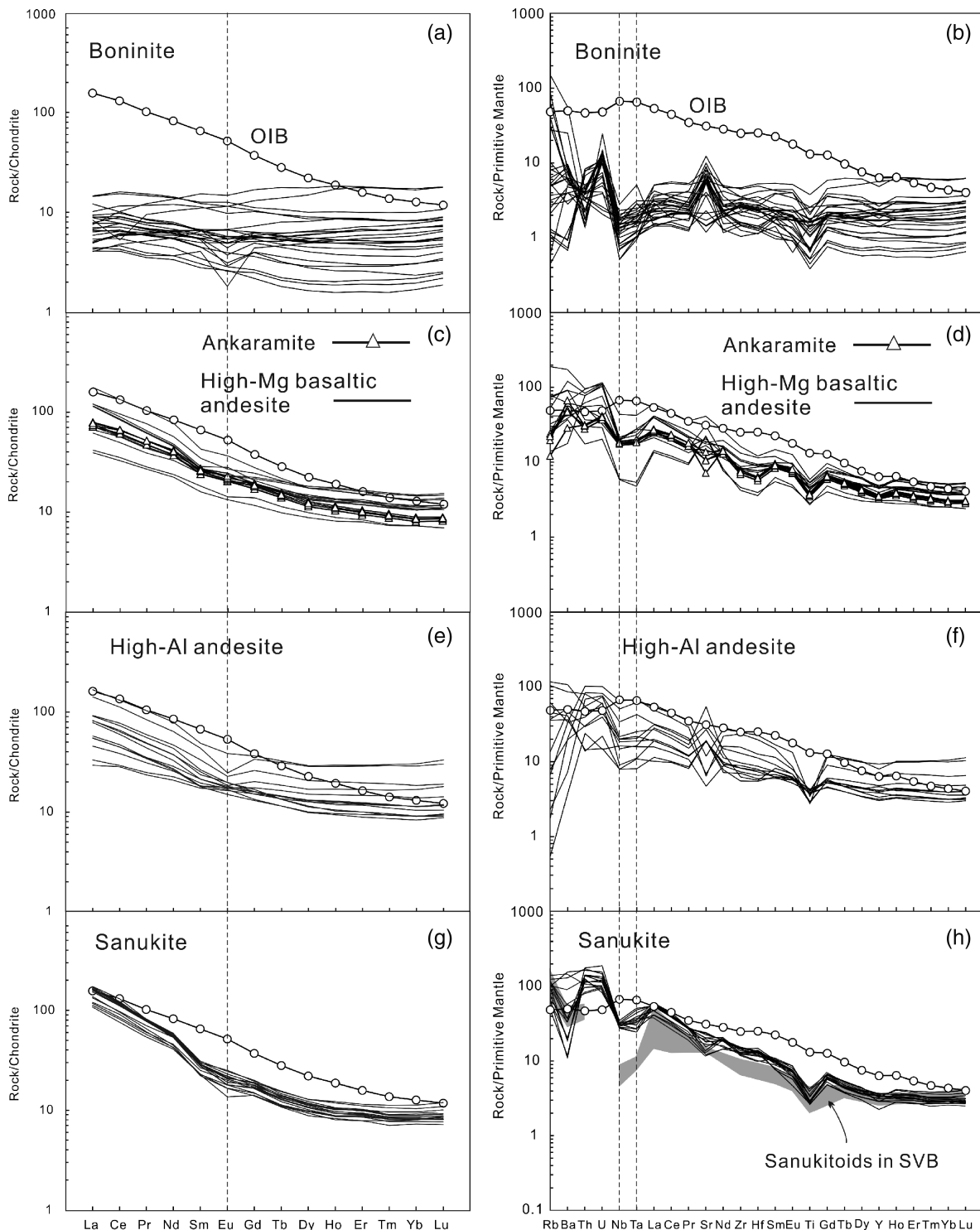


Fig. 4. Chondrite-normalized REE patterns (a, c, e, g) and primitive mantle (PM)-normalized multi-element patterns (b, d, f, h) for the Lajishan–Yongjing island arc volcanic rocks. Normalization and OIB values are from Sun & McDonough (1989). Data for sanukitoids from the Setouchi Volcanic Belt (SVB), used for comparison, are from Tatsumi & Hanyu (2003).

depleted in Ba, Sr and HFSE (Nb, Ta and Ti) and enriched in LILE (e.g. Rb, Th, U and Pb). Therefore, these lavas have similar major and trace element compositions to sanukite ($\text{SiO}_2 = 55\text{--}60$ wt %; $\text{Mg}\# > 0.6$; $\text{K}_2\text{O} > 1$ wt %; $\text{Cr} > 200$ ppm; $\text{Ni} > 100$ ppm; $\text{Ba} > 500$ ppm; $\text{Sr} > 500$ ppm; Stern *et al.*, 1989; Tatsumi, 2006).

Mineral chemistry

Samples of primitive lavas from the Lajishan–Yongjing island arc volcanic complex were chosen to characterize mineral compositions, including Cr-spinel and Cpx from two Cpx-phyric ankaramites (13QLS-68 and 13QLS-72), two high-Mg basaltic andesites (13QLS-124 and

LJ15-42) and two boninites (LJ15-12 and LJ15-15). The representative compositions for major elements and trace elements are given in Table 2 and Supplementary Data Appendix Tables 1–3 (supplementary data are available for downloading at <http://www.petrology.oxfordjournals.org>).

Chromian spinel

Spinels from boninites are characterized by high Cr# [$\text{Cr}/(\text{Cr} + \text{Al}) = 75.3\text{--}90.6$], and low Al_2O_3 and TiO_2 contents, with normal to evolved Mg# [$\text{Mg}/(\text{Fe}^{2+} + \text{Mg})$] varying from cores of 35.63–52.90 to rims of 1.45–22.60 (Fig. 5). Spinels from ankaramite samples are characterized by relative lower Cr# [$\text{Cr}/(\text{Cr} + \text{Al}) = 68.5\text{--}81.9$], and higher Al_2O_3 and TiO_2 contents than those from boninite, with normal to evolved Mg# varying from 1.74 to 43.66 (Fig. 5). Spinels from ankaramites can be subdivided in two groups: the chromian spinel grains from the matrix and the chromian spinel inclusions in Cpx grains. Spinel grains in the matrix have higher Cr# (69.6–90.6), higher TiO_2 , and lower Mg# and Al_2O_3 than inclusions in Cpx, which may result from mineral–melt interaction (Cao *et al.*, 2016).

Clinopyroxene

Cpx phenocrysts are mostly Ca-rich Cpx with a formula of $\text{Wo}_{38\text{--}47}\text{En}_{43\text{--}50}\text{Fs}_{5\text{--}16}$ and Mg# varying from 76 to 94. Cpx from primitive samples (13QLS-68, 13QLS-72 and LJ15-42) has high Mg# (87–94) and Cr# (12–25), and high contents of SiO_2 (51.74–53.27 wt %) and CaO (21.94–22.36 wt %), but low contents of TiO_2 (0.13–0.45 wt %), Al_2O_3 (1.75–3.45 wt %), FeO (3.67–4.67 wt %) and Na_2O (0.20–0.29 wt %). In contrast, two kinds of Cpx grains occur in the evolved sample (13QLS-124), including homogeneous low-Mg# grains and recrystallized Cpx grains exhibiting core–rim structure with a high-Mg# core and low-Mg# rim. The cores of the recrystallized Cpx grains have higher Mg#, Cr#, SiO_2 and CaO, but lower TiO_2 , Al_2O_3 and FeO_T than either the rims of recrystallized Cpx or low Mg# Cpx grains, corresponding to the high Mg# Cpx grains in primitive samples (Fig. 6). The Mg# of Cpx shows positive correlation with SiO_2 , CaO and Cr#, and negative correlation with TiO_2 , Al_2O_3 and Na_2O contents (Fig. 6).

Trace elements in Cpx grains (Supplementary Data Appendix Table 3) are characterized by depletions in LREE with $(\text{La}/\text{Sm})_N = 0.34\text{--}0.61$ and gently fractionated heavy rare earth elements (HREE) with $(\text{Dy}/\text{Yb})_N = 1.12\text{--}2.21$. Cpx rims from the sample 13QLS-124 (Mg# = 69) have higher trace element contents than the cores (Mg# = 89–93), whereas the Cpx compositions from sample 13QLS-72 (Mg# = 77) are relative homogeneous and similar to (or have slightly high Mg# than) the Cpx cores in sample 13QLS-124. In a primitive mantle-normalized trace element pattern, the Cpx cores are characterized by negative anomalies in Nb, Zr, Hf and Ti, and variable enrichments in Rb, Sr, Pb, Th and U, whereas the rims show strongly negative Sr anomalies

(Supplementary Data Fig. S1). To further estimate the parental magmas of the Cpx-phyric basaltic andesite, we used Cpx/basalt partition coefficients to calculate the primary melt compositions as described by Tang *et al.* (2012) and references therein. The back-calculated melt concentrations for the Cpx cores with the highest Mg# from sample 13QLS-124 are considered as the primary melt compositions (Supplementary Data Appendix Table 3).

Whole-rock Sr–Nd isotopes

We selected samples with the lowest LOI values to minimize the influence on the Sr isotope compositions of alteration or low-grade metamorphism. Whole-rock Sr–Nd isotopic data for the Lajishan–Yongjing island arc volcanic complex are given in Table 3. Initial Sr isotopic ratios and $\epsilon_{\text{Nd}}(t)$ values are calculated at $t = 450$ Ma based on the zircon U–Pb dating. Seven boninite samples have variable initial $^{87}\text{Sr}/^{86}\text{Sr}$ ratios of 0.7041–0.7056 and $\epsilon_{\text{Nd}}(t)$ values of 1.80–8.39. Two ankaramite samples exhibit relatively constant initial $^{87}\text{Sr}/^{86}\text{Sr}$ ratios of 0.7050–0.7052 and $\epsilon_{\text{Nd}}(t)$ values of 2.46–2.78. Four high-Mg basaltic andesite samples show a narrow range of initial $^{87}\text{Sr}/^{86}\text{Sr}$ from 0.7046 to 0.7053 and $\epsilon_{\text{Nd}}(t)$ values of 0.95–2.78. Two high-Al andesite samples show relatively constant initial $^{87}\text{Sr}/^{86}\text{Sr}$ ratios of 0.7050–0.7053 and $\epsilon_{\text{Nd}}(t)$ values of 1.69–2.7. They exhibit covariation between Sr and Nd isotopes. Six sanukite samples show a range of initial $^{87}\text{Sr}/^{86}\text{Sr}$ of 0.7061–0.7073 and $\epsilon_{\text{Nd}}(t)$ values of –2.07 to –5.66. Two coeval metasedimentary samples, occurring as interlayers within volcanic rocks, show initial $^{87}\text{Sr}/^{86}\text{Sr}$ ratios of 0.7098 and $\epsilon_{\text{Nd}}(t)$ values of –6.73 to –7.40. It should be noted that the relatively high initial Sr isotopic values of some samples indicate that the Sr isotopes may be influenced by the variable degree of alteration. However, the influence is insignificant, given that these samples form a tight cluster in the Sr–Nd diagram (see below). Instead, all the Sr–Nd isotopic data for volcanic samples overlap the transition field, showing the possibility of mixing between an enriched mantle source and oceanic sediments.

Zircon U–Pb ages

Six volcanic samples from the Lajishan–Yongjing Terrane were selected for LA-ICP-MS and SIMS zircon U–Pb dating, including a boninite (LJ15-01), a high-Mg basaltic andesite (16LJ-27), a high-Al andesite (LJ15-70) and three sanukite samples (12LJ-15, 16LJ-55 and 16LJ-69). The CL images of representative zircon grains are illustrated in Supplementary Data Fig. S2, and the zircon U–Pb isotope data are plotted in Fig. 7 and listed in Supplementary Data Appendix Table 4. All zircons are subhedral to euhedral, colorless and transparent, and have grain sizes of 30–300 μm with length-to-width ratios of 1:1 to 3:1. Zircons from sanukite samples (16LJ-55 and 16LJ-69) show oscillatory or banded zoning, whereas zircons from the other samples exhibit broad oscillatory zoning, or weak or no obvious zoning in the CL

Table 2: Average electron microprobe analyses of Cpx for Lajishan–Yongjing arc volcanic rocks

Sample	n	SiO ₂	TiO ₂	Al ₂ O ₃	Cr ₂ O ₃	FeO _T	MnO	MgO	CaO	Na ₂ O	K ₂ O	Total	Si	Al(IV)	Al(VI)	Ti	Cr	Fe ³⁺	Fe ²⁺	Mn	Mg	Ca	Na	K	Sum	Wo	En	Fs	Ac	Mg#
13QLS68-1	3	53.27	0.13	1.75	0.85	3.67	0.14	17.48	22.15	0.22	0.00	99.65	1.95	0.05	0.02	0.00	0.02	0.02	0.10	0.00	0.95	0.87	0.02	0.00	4.01	44.45	48.79	5.97	0.78	0.91
13QLS68-2	10	52.70	0.29	2.17	0.82	4.33	0.13	16.83	22.36	0.22	0.01	99.66	1.93	0.07	0.03	0.01	0.02	0.03	0.11	0.00	0.92	0.88	0.02	0.00	4.01	45.03	47.16	7.00	0.82	0.90
13QLS68-3	4	52.74	0.22	2.18	0.74	3.90	0.12	16.90	21.94	0.25	0.00	98.99	1.94	0.06	0.04	0.01	0.02	0.01	0.11	0.00	0.93	0.87	0.02	0.00	4.00	44.73	47.94	6.40	0.93	0.89
13QLS68-4	3	52.07	0.43	2.93	0.66	4.67	0.15	16.06	22.01	0.29	0.00	99.27	1.92	0.08	0.05	0.01	0.02	0.01	0.13	0.00	0.88	0.87	0.02	0.00	4.00	45.25	45.95	7.73	1.08	0.87
13QLS68-5	7	53.11	0.22	2.24	0.79	4.08	0.12	16.65	22.30	0.21	0.01	99.74	1.94	0.06	0.04	0.01	0.02	0.01	0.12	0.00	0.91	0.87	0.02	0.00	4.00	45.39	47.14	6.68	0.79	0.89
13QLS68-6	6	52.61	0.35	2.63	0.64	4.56	0.14	16.37	22.29	0.24	0.00	99.84	1.93	0.07	0.04	0.01	0.02	0.01	0.13	0.00	0.90	0.88	0.02	0.00	4.00	45.33	46.33	7.45	0.88	0.88
13QLS72-1	5	51.74	0.45	3.45	0.62	4.66	0.11	15.76	22.02	0.25	0.20	99.26	1.91	0.09	0.06	0.01	0.02	0.02	0.13	0.00	0.87	0.87	0.02	0.01	4.01	45.78	45.50	7.78	0.94	0.87
13QLS72-3	3	52.49	0.30	2.37	0.63	4.51	0.16	16.50	22.01	0.21	0.01	99.19	1.94	0.06	0.04	0.01	0.02	0.01	0.13	0.00	0.91	0.87	0.02	0.00	4.00	44.93	46.85	7.43	0.79	0.87
13QLS72-7	2	52.31	0.31	2.79	0.90	4.08	0.16	16.41	22.14	0.27	0.00	99.35	1.92	0.08	0.05	0.01	0.03	0.01	0.12	0.00	0.90	0.87	0.02	0.00	4.00	45.41	46.82	6.79	0.99	0.88
13QLS72-9	5	52.94	0.24	2.04	0.50	4.26	0.13	16.73	22.19	0.20	0.01	99.23	1.95	0.05	0.04	0.01	0.01	0.01	0.12	0.00	0.92	0.87	0.01	0.00	4.00	45.04	47.26	6.95	0.75	0.88
13QLS124-1	10	50.08	0.66	3.29	0.26	8.18	0.23	15.31	19.56	0.27	0.02	97.87	1.90	0.10	0.04	0.02	0.01	0.05	0.21	0.01	0.86	0.79	0.02	0.00	4.02	40.85	44.47	13.66	1.03	0.81
13QLS124-2	6	49.69	0.71	3.44	0.13	9.01	0.27	15.11	18.85	0.30	0.00	97.50	1.89	0.11	0.05	0.02	0.00	0.05	0.23	0.01	0.86	0.77	0.02	0.00	4.02	39.57	44.13	15.15	1.15	0.79
13QLS124-3	6	51.84	0.37	2.01	0.56	5.40	0.17	16.69	21.12	0.22	0.01	98.37	1.93	0.07	0.02	0.01	0.02	0.03	0.14	0.01	0.93	0.84	0.02	0.00	4.01	43.02	47.28	8.91	0.80	0.87
LJ15-42-1	2	53.02	0.38	2.47	0.90	3.85	0.12	17.29	21.91	0.28	0.01	100.21	1.93	0.07	0.04	0.01	0.03	0.01	0.10	0.00	0.94	0.85	0.02	0.00	4.00	44.23	48.53	6.24	1.01	0.90
LJ15-42-2	2	52.39	0.43	3.19	1.06	4.06	0.11	16.93	21.58	0.33	0.00	100.05	1.91	0.09	0.05	0.01	0.03	0.02	0.11	0.00	0.92	0.84	0.02	0.00	4.00	44.06	48.10	6.64	1.22	0.90
LJ15-42-3	2	53.34	0.38	2.26	0.01	5.17	0.24	17.43	21.04	0.18	0.01	100.04	1.95	0.05	0.04	0.01	0.00	0.00	0.15	0.01	0.95	0.82	0.01	0.00	4.00	42.23	48.66	8.46	0.66	0.86
LJ15-42-4	2	53.07	0.26	2.26	0.79	3.77	0.14	17.25	22.00	0.27	0.01	99.80	1.94	0.06	0.04	0.01	0.02	0.01	0.10	0.00	0.94	0.86	0.02	0.00	4.00	44.42	48.46	6.15	0.97	0.90
LJ15-42-5	2	53.12	0.32	2.55	1.00	3.70	0.10	17.23	21.84	0.30	0.01	100.15	1.93	0.07	0.04	0.01	0.03	0.01	0.10	0.00	0.93	0.85	0.02	0.00	4.00	44.29	48.61	6.01	1.10	0.90
LJ15-42-6	2	52.89	0.31	2.49	0.86	3.91	0.13	17.31	21.79	0.31	0.00	99.98	1.93	0.07	0.04	0.01	0.02	0.02	0.10	0.00	0.94	0.85	0.02	0.00	4.01	43.97	48.58	6.35	1.11	0.91
LJ15-42-7	2	52.42	0.41	3.15	1.08	3.70	0.09	16.76	22.17	0.26	0.00	100.02	1.91	0.09	0.05	0.01	0.03	0.01	0.11	0.00	0.91	0.87	0.02	0.00	4.00	45.34	47.67	6.05	0.95	0.90
LJ15-42-8	2	52.98	0.35	2.66	0.85	3.82	0.16	16.91	21.84	0.25	0.00	99.81	1.93	0.07	0.05	0.01	0.02	0.01	0.11	0.00	0.92	0.85	0.02	0.00	4.00	44.65	48.08	6.35	0.93	0.89
LJ15-42-9	3	52.37	0.50	3.12	0.87	4.07	0.12	16.73	22.05	0.27	0.01	100.10	1.91	0.09	0.05	0.01	0.03	0.02	0.11	0.00	0.91	0.86	0.02	0.00	4.00	44.94	47.43	6.66	0.98	0.89
LJ15-42-10	3	52.71	0.31	2.71	1.04	3.92	0.11	17.17	21.64	0.30	0.00	99.92	1.92	0.08	0.04	0.01	0.03	0.01	0.11	0.00	0.93	0.85	0.02	0.00	4.00	43.98	48.54	6.38	1.09	0.90
LJ15-42-11	1	52.84	0.32	3.11	1.24	3.59	0.12	16.67	21.96	0.33	0.00	100.18	1.92	0.08	0.06	0.01	0.04	0.00	0.11	0.00	0.90	0.86	0.02	0.00	4.00	45.14	47.67	5.96	1.23	0.89
LJ15-42-12	2	52.58	0.44	2.90	1.03	4.12	0.19	16.69	21.86	0.29	0.00	100.08	1.92	0.08	0.04	0.01	0.03	0.00	0.12	0.01	0.91	0.85	0.02	0.00	4.00	44.65	47.43	6.87	1.05	0.88
LJ15-42-13	2	53.08	0.29	3.38	0.52	4.68	0.18	16.74	21.01	0.44	0.00	100.30	1.93	0.07	0.07	0.01	0.01	0.00	0.14	0.01	0.91	0.82	0.03	0.00	4.00	42.97	47.65	7.77	1.63	0.87

Table 3: Whole-rock Rb–Sr and Sm–Nd isotope compositions for the Lajishan–Yongjing arc volcanic rocks

Sample no.	Rock type	t (Ma)	Rb	Sr	$^{87}\text{Rb}/^{86}\text{Sr}$	$^{87}\text{Sr}/^{86}\text{Sr}$	2σ	t_{Sr} (t)	Sm	Nd	$^{147}\text{Sm}/^{144}\text{Nd}$	$^{143}\text{Nd}/^{144}\text{Nd}$	2σ	$f_{\text{Sm}/\text{Nd}}$	$^{143}\text{Nd}/^{144}\text{Nd}(t)$	$\epsilon_{\text{Nd}}(0)$	$\epsilon_{\text{Nd}}(t)$
LJ15-01	Boninite	450	1.5	494.0	0.0088	0.704924	0.000006	0.7049	1.3	4.0	0.19	0.512801	0.000005	-0.03	0.512237	-7.8	3.48
LJ15-12	Boninite	450	17.6	171.4	0.2964	0.706957	0.000004	0.7051	1.9	6.8	0.17	0.512989	0.000018	-0.13	0.512488	-2.9	8.39
LJ15-13	Boninite	450	3.1	140.4	0.0638	0.706051	0.000009	0.7056	0.9	3.2	0.18	0.512740	0.000012	-0.10	0.512220	-8.1	3.17
LJ15-14	Boninite	450	0.4	261.2	0.0043	0.704805	0.000005	0.7048	2.4	6.4	0.22	0.513127	0.000006	0.14	0.512467	-3.3	7.98
LJ15-108	Boninite	450	4.0	152.0	0.0763	0.706052	0.000007	0.7056	1.3	4.3	0.18	0.512679	0.000010	-0.09	0.512151	-9.5	1.80
12LJ-07	Boninite	450	41.3	85.9	1.3583	0.713346	0.000017	0.7046	0.9	2.9	0.18	0.512752	0.000019	-0.06	0.512209	-8.4	2.94
12LJ-09	Boninite	450	55.5	122.0	1.2838	0.712350	0.000018	0.7041	1.0	3.6	0.18	0.512772	0.000014	-0.10	0.512253	-7.5	3.80
13QLS-68	Ankaramite	450	15.2	225.8	0.1942	0.706281	0.000010	0.7050	3.7	17.4	0.13	0.512578	0.000010	-0.35	0.512200	-8.5	2.78
13QLS-70	Ankaramite	450	12.3	221.4	0.1611	0.706210	0.000006	0.7052	4.0	18.9	0.13	0.512556	0.000012	-0.36	0.512184	-8.9	2.46
LJ15-40	HMBA	450	33.5	370.8	0.2615	0.706338	0.000010	0.7047	4.4	22.2	0.12	0.512524	0.000005	-0.40	0.512175	-9.0	2.27
LJ15-42	HMBA	450	46.2	399.0	0.3347	0.706750	0.000009	0.7046	4.2	21.4	0.12	0.512461	0.000002	-0.40	0.512115	-10.2	1.11
LJ15-166	HMBA	450	17.7	651.4	0.0784	0.705760	0.000007	0.7053	3.9	16.8	0.14	0.512522	0.000003	-0.28	0.512107	-10.4	0.95
16LJ-27	HMBA	450	15.3	458.6	0.0967	0.705711	0.000007	0.7051	2.4	10.4	0.14	0.512531	0.000003	-0.28	0.512113	-10.2	1.07
13QLS-100	HAA	450	23.4	1154.2	0.0586	0.705336	0.000007	0.7050	3.6	17.5	0.12	0.512565	0.000003	-0.37	0.512197	-8.6	2.70
13QLS-103	HAA	450	74.1	569.6	0.3759	0.707711	0.000006	0.7053	3.3	15.3	0.13	0.512526	0.000002	-0.34	0.512145	-9.6	1.69
LJ15-53	Sanukite	450	63.7	498.0	0.3695	0.709438	0.000008	0.7071	4.6	25.7	0.11	0.512086	0.000003	-0.45	0.511769	-17.0	-5.66
LJ15-54	Sanukite	450	79.0	432.4	0.5284	0.710103	0.000008	0.7067	4.1	24.9	0.10	0.512244	0.000007	-0.50	0.511952	-13.4	-2.07
LJ15-55	Sanukite	450	39.8	388.4	0.2965	0.709206	0.000008	0.7073	4.4	25.2	0.10	0.512180	0.000005	-0.47	0.511871	-15.0	-3.66
16LJ-69	Sanukite	450	31.4	257.8	0.3516	0.708843	0.000007	0.7066	3.5	19.7	0.11	0.512170	0.000003	-0.46	0.511857	-15.2	-3.94
12LJ13	Sanukite	450	63.5	283.2	0.6335	0.710690	0.000017	0.7066	4.5	27.5	0.10	0.512174	0.000014	-0.48	0.511871	-15.0	-3.66
12LJ15	Sanukite	450	61.0	264.2	0.6524	0.710295	0.000018	0.7061	4.4	25.0	0.11	0.512215	0.000012	-0.43	0.511884	-14.7	-3.39
LJ15-76	Sediments	450	97.4	106.3	2.6487	0.726746	0.000006	0.7098	3.7	19.9	0.11	0.512045	0.000002	-0.43	0.511714	-18.0	-6.73
LJ15-77	Sediments	450	112.8	234.0	1.3937	0.718771	0.000006	0.7098	5.1	28.0	0.11	0.512004	0.000006	-0.44	0.511679	-18.7	-7.40

$t_{\text{Sr}} = \frac{^{87}\text{Sr}/^{86}\text{Sr} - ^{87}\text{Rb}/^{86}\text{Sr} \times (e^{\lambda_{\text{Sr}}} - 1)}{\lambda_{\text{Sr}}}$, where $\lambda_{\text{Sr}} = 1.3972 \times 10^{-11} \text{ a}^{-1}$ (IUPAC; Villa *et al.*, 2015). $\epsilon_{\text{Nd}}(t) = \left[\frac{^{143}\text{Nd}/^{144}\text{Nd}}{^{143}\text{Nd}/^{144}\text{Nd}}_{\text{CHUR}} - 1 \right] \times 10^4$, where $\lambda_{\text{Nd}} = 6.54 \times 10^{-12} \text{ a}^{-1}$, $(^{143}\text{Nd}/^{144}\text{Nd})_{\text{CHUR}} = 0.512638$ and $(^{147}\text{Sm}/^{144}\text{Nd})_{\text{CHUR}} = 0.1967$ (Jacobsen & Wasserburg, 1980). HMBA, high-Mg basaltic andesite; HAA, high-Al andesite.

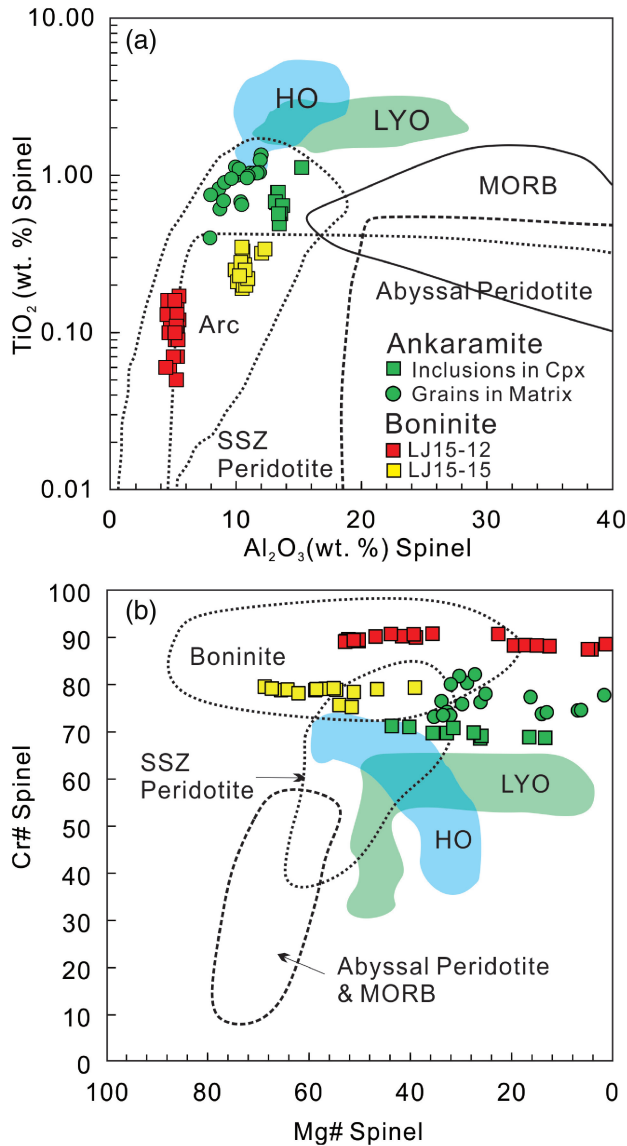


Fig. 5. Compositional variations of Cr-spinel in island arc volcanic rocks from the Lajishan–Yongjing Terrane. (a) Al₂O₃ vs TiO₂ (Kamenetsky *et al.*, 2001); (b) Cr# vs Mg# (Dick & Bullen, 1984). Cr-spinel data for the Lajishan–Yongjing Ophiolite (LYO) and Hawaiian OIB (HO) are from Zhang *et al.* (2017) and reference therein. SSZ, suprasubduction zone.

images (Supplementary Data Fig. S1). As shown in Supplementary Data Appendix Table 4, most zircon U–Pb isotope data are concordant within analytical error.

Zircon U–Pb isotopic analyses from boninite sample LJ15-01 by SIMS show highly variable Th (118–2693 ppm) and U contents (67–4050 ppm) with high Th/U ratios (0.22–2.79). Nineteen analyses give a weighted ²⁰⁶Pb/²³⁸U mean age of 450 ± 6 Ma (MSWD = 2.3, *n* = 16), with three relict zircons aged 523–1701 Ma (Fig. 7a).

Zircons from the high-Mg basaltic andesite sample (16LJ-27) have moderate Th (45–258 ppm) and U (115–472 ppm) contents and high Th/U ratios (0.65–1.35).

Thirty analyses yield a concordia age of 456 ± 1 Ma (MSWD = 0.36, *n* = 30) (Fig. 7b).

Zircons from the high-Al andesite sample (LJ15-70) have variable Th (117–1641 ppm) and U contents (222–831 ppm) with Th/U ratios of 0.45–2.66. Seventeen analyses by SIMS give a concordia age of 452 ± 1 Ma (MSWD = 0.95, *n* = 17), and one relict zircon grain yields a ²⁰⁶Pb/²³⁸U age of 774 ± 11 Ma (Fig. 7c).

Zircons from the three sanukite samples (12LJ-15, 16LJ-55 and 16LJ-69) were analyzed by LA-ICP-MS. They have consistent contents of U (183–570 ppm) and Th (108–394 ppm), with high Th/U ratios of 0.44–1.12. Twenty-five analyses of zircon grains from 12LJ-15 yield a concordia age of 440 ± 1 Ma (MSWD = 0.61) (Fig. 7d). Twenty-six analyses of 29 zircon grains from 16LJ-55 define a concordia age of 448 ± 1 Ma (MSWD = 0.54), apart from three strongly discordant ages, which may due to lead loss (Fig. 7e). Twenty-two analyses of 25 zircon grains from 16LJ-69 yield a concordia age of 455 ± 1 Ma (MSWD = 0.52), with three relict zircon ages (Fig. 7f).

In summary, the U–Pb dating on magmatic zircon domains for the Lajishan–Yongjing arc volcanic complex yields consistent ages of 456–440 Ma, implying that the Lajishan–Yongjing island arc was formed in a relatively short period during the Late Ordovician, much younger than the ages of the adjacent ophiolite complex (~525 Ma; Zhang *et al.*, 2017). Relict zircons are rare, suggesting insignificant assimilation of continental crust.

Zircon Hf–O isotopes

Zircon Hf isotopic data for the Lajishan–Yongjing island arc complex are given in Supplementary Data Appendix Table 5. Zircons from the high-Mg basaltic andesite (sample 16LJ-27) have a narrow range of initial ¹⁷⁶Hf/¹⁷⁷Hf (0.282819–0.282874) and the calculated $\epsilon_{\text{Hf}}(t)$ (where *t* = 456 Ma) values range from 11.69 to 15.38, with a weighted mean of 13.72 ± 0.57 (MSWD = 1.4, *n* = 16). Zircons from the two sanukite samples (16LJ-55 and 16LJ-69) have uniform initial ¹⁷⁶Hf/¹⁷⁷Hf ratios (0.282300–0.282569) and the calculated $\epsilon_{\text{Hf}}(t)$ values range from –3.22 to 0.44, with a weighted mean of –0.27 ± 0.43 (MSWD = 1.4, *n* = 16) and from –2.11 to 1.62 with a weighted mean of –0.60 ± 0.43 (MSWD = 2.2, *n* = 16), respectively. It is notable that the Hf isotopic compositions of the island arc complex are decoupled from the Nd isotopic compositions, showing various positive $\Delta\epsilon_{\text{Hf}}(t)$ values of 10.85 for sample 16LJ-27, 4.20 for sample 16LJ-55, and 4.30 for sample 16LJ-69 [$\Delta\epsilon_{\text{Hf}}(t) = \epsilon_{\text{Hf}}(t) - 1.55\epsilon_{\text{Nd}}(t) - 1.21$; Vervoort *et al.*, 2011].

Zircon O isotopic data for the Lajishan–Yongjing island arc complex are given in Table 4. The $\delta^{18}\text{O}$ values for zircons from boninite (LJ15-01) mostly range from 6.57 to 7.61‰, with a weighted mean of 7.17 ± 0.13‰ (MSWD = 9.5, *n* = 17). Zircons from high-Al andesite (LJ15-70) mostly have uniform $\delta^{18}\text{O}$ values of 5.4–6.24‰, with a weighted mean of 5.90 ± 0.09‰

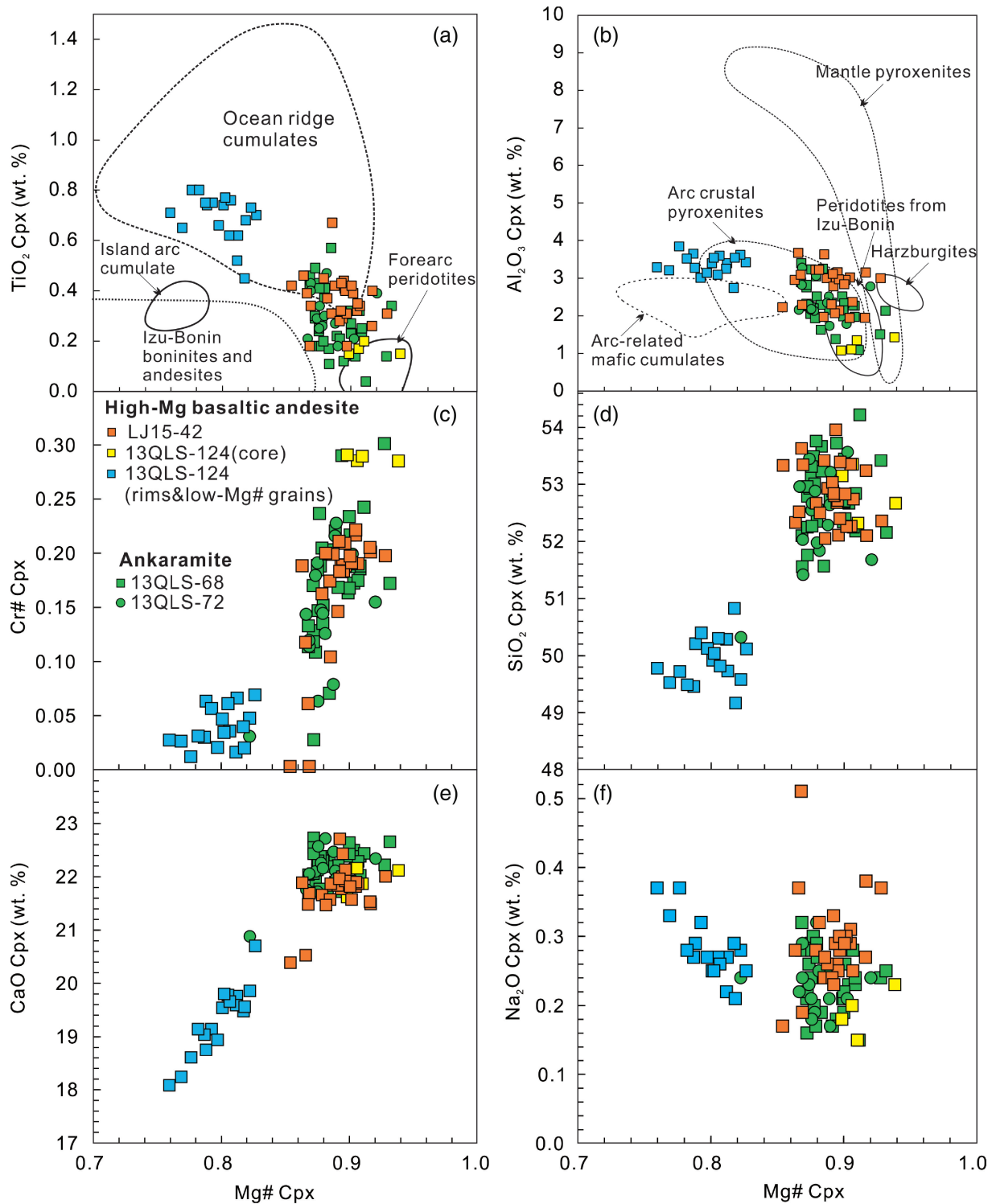


Fig. 6. Compositional variations of Cpx in island arc volcanic rocks from the Lajishan–Yongjing Terrane. Fields of Cpx compositions for ocean ridge cumulates, Izu–Bonin arc volcanic rocks, island arc cumulates (lower crustal gabbroanorites) and depleted fore-arc peridotites are from Marchesi *et al.* (2009) and references therein.

(MSWD = 5.6, $n = 18$). The estimated whole-rock $\delta^{18}\text{O}$ values roughly range from 7.44 to 8.49‰ (mean of $8.05 \pm 0.13\text{‰}$) for LJ15-01, and from 6.23 to 7.06‰ (mean of $6.73 \pm 0.09\text{‰}$) for LJ15-70 [$\delta^{18}\text{O}_{\text{WR}} = \delta^{18}\text{O}_{\text{Zir}} + 0.0612$ (wt % SiO_2) – 2.5; Valley *et al.*, 2005].

DISCUSSION

Petrogenesis of the arc volcanic complex

Crustal assimilation or source mixing

The compositions of primitive arc magmas are determined by the composition of the mantle source, the

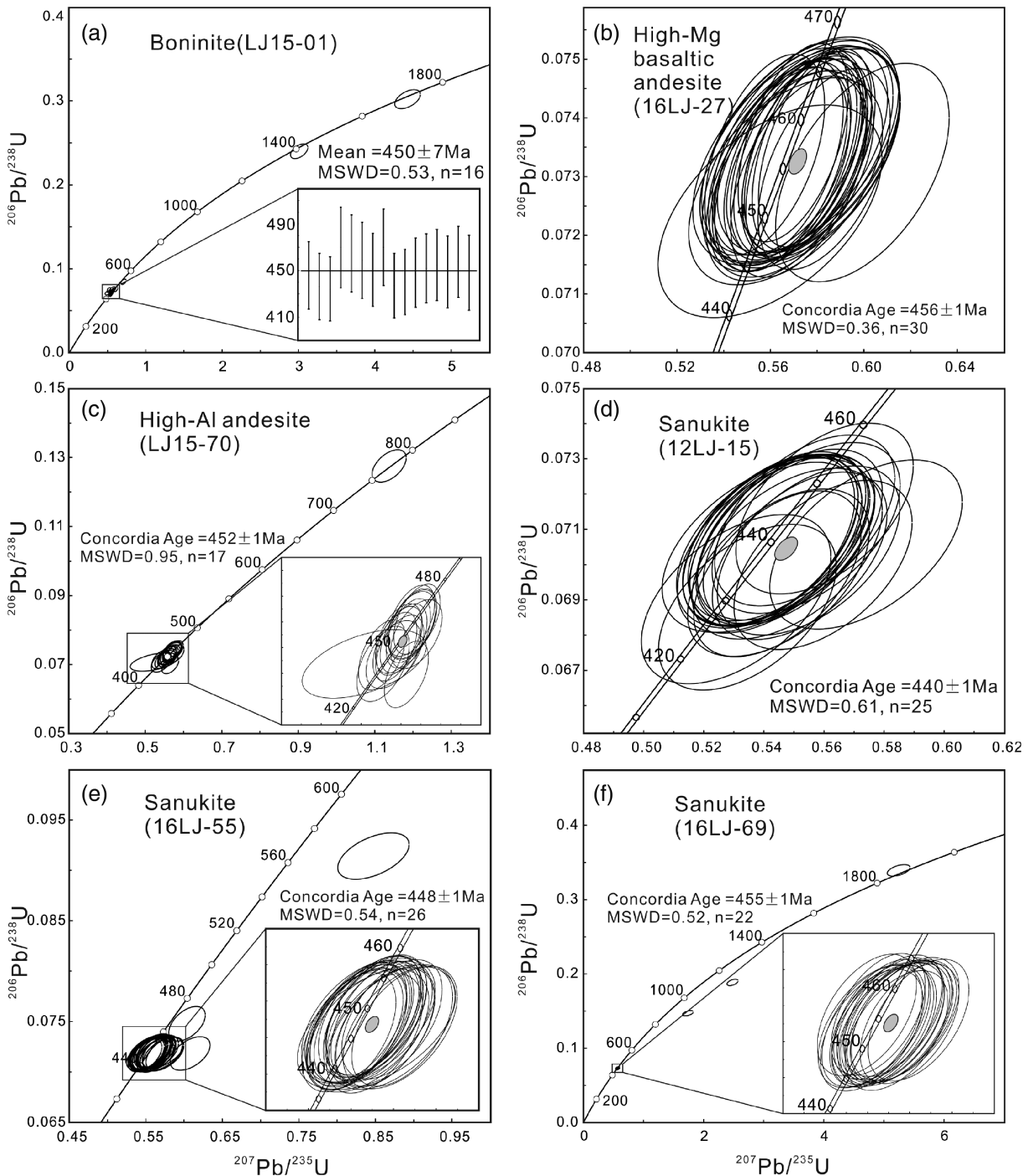


Fig. 7. Concordia diagrams of zircon U–Pb isotope data analyzed with SIMS and LA-ICP-MS for island arc volcanic rocks from the Lajishan–Yongjing Terrane.

slab-derived components (including fluids and melts) and the P – T conditions of partial melting, and can be influenced by a number of factors, such as shallow-level crustal assimilation and fractional crystallization (AFC). Generally, source mixing and crustal assimilation are the two fundamental mechanisms for the incorporation of crustal components into mantle-derived magmas, and thus are capable of producing variations in the elemental and isotopic compositions of arc magmas

(Zheng & Hermann, 2014; Bezard *et al.*, 2015). In contrast, simple fractional crystallization can also occur during arc magma ascent that produces rock types with variations in the major and trace element compositions, but does not affect the isotopic compositions.

As shown in Figs 8 and 9, boninite samples have distinct characteristics (e.g. low La/Sm and TiO₂) and evolutionary trends from the other rock types, suggesting they were derived from different sources in the mantle

Table 4: In situ zircon O isotopic data for the Lajishan–Yongjing island arc volcanic rocks

Sample	$^{16}\text{O}/^{18}\text{O}_{\text{Mean}}$	$\delta^{18}\text{O}$ (‰) _{ZIR}	$\pm 2\sigma$	$\delta^{18}\text{O}$ (‰) _{WR}	$\pm 2\sigma$
LJ15-01@1	0.002023	6.97	0.13	7.84	0.13
LJ15-01@2	0.002022	6.70	0.14	7.58	0.14
LJ15-01@3	0.002024	7.47	0.14	8.34	0.14
J15-01@4	0.002023	7.20	0.15	8.08	0.15
LJ15-01@5	0.002019	5.82	0.17	6.69	0.17
LJ15-01@6	0.002018	4.66	0.26	5.53	0.26
LJ15-01@7	0.002024	7.61	0.17	8.49	0.17
LJ15-01@8	0.002026	8.63	0.14	9.50	0.14
LJ15-01@9	0.002023	7.35	0.14	8.22	0.14
LJ15-01@10	0.002024	7.59	0.21	8.46	0.21
LJ15-01@11	0.002023	7.20	0.27	8.08	0.27
LJ15-01@12	0.002023	7.13	0.19	8.00	0.19
LJ15-01@13	0.002023	7.06	0.20	7.93	0.20
LJ15-01@14	0.002022	6.57	0.31	7.44	0.31
LJ15-01@15	0.002023	7.09	0.16	7.97	0.16
LJ15-01@16	0.002024	7.43	0.21	8.30	0.21
LJ15-01@17	0.002023	7.17	0.16	8.04	0.16
LJ15-01@18	0.002023	7.22	0.19	8.09	0.19
LJ15-01@19	0.002023	6.96	0.16	7.84	0.16
LJ15-01@20	0.002023	7.21	0.15	8.08	0.15
LJ15-70@1	0.002019	5.73	0.12	6.56	0.12
LJ15-70@2	0.002021	6.85	0.18	7.68	0.18
LJ15-70@3	0.002015	3.86	0.35	4.68	0.35
LJ15-70@4	0.002026	9.33	0.20	10.16	0.20
LJ15-70@5	0.002020	6.04	0.09	6.86	0.09
LJ15-70@6	0.002020	5.96	0.21	6.79	0.21
LJ15-70@7	0.002018	5.40	0.19	6.23	0.19
LJ15-70@8	0.002019	5.74	0.26	6.57	0.26
LJ15-70@9	0.002020	6.09	0.21	6.92	0.21
LJ15-70@10	0.002019	5.74	0.19	6.57	0.19
LJ15-70@11	0.002019	5.77	0.12	6.60	0.12
LJ15-70@12	0.002019	5.61	0.18	6.44	0.18
LJ15-70@13	0.002016	4.16	0.26	4.98	0.26
LJ15-70@14	0.002019	5.81	0.14	6.64	0.14
LJ15-70@15	0.002019	5.88	0.22	6.71	0.22
LJ15-70@16	0.002020	6.04	0.08	6.87	0.08
LJ15-70@17	0.002020	5.96	0.17	6.79	0.17
LJ15-70@18	0.002020	6.02	0.19	6.85	0.19
LJ15-70@19	0.002020	6.00	0.28	6.83	0.28
LJ15-70@20	0.002019	5.81	0.25	6.64	0.25
LJ15-70@21	0.002020	6.24	0.20	7.06	0.20
LJ15-70@22	0.002019	5.80	0.20	6.63	0.20

$$\delta^{18}\text{O}_{\text{WR}} = \delta^{18}\text{O}_{\text{Zir}} + 0.0612 (\text{wt } \% \text{ SiO}_2) - 2.5 \text{ (Valley et al., 2005)}.$$

wedge. The other four types of rocks show positive correlations between La/Sm versus La and SiO₂ content (Fig. 8a and b), indicating that the partial melting of metasomatized mantle or crustal contamination during ascent could readily explain the petrogenesis of the volcanic rocks. The sanukite has lowest $\epsilon_{\text{Nd}}(t)$ and highest ($^{87}\text{Sr}/^{86}\text{Sr}$)_i, and is likely to have undergone a high degree of source metasomatism or crustal assimilation relative to other samples (Fig. 8c and d). In contrast, the boninite lavas exhibit high $\epsilon_{\text{Nd}}(t)$ and low La/Sm ratios relative to other rock types, suggesting that they are derived from a more depleted mantle source with the least source metasomatism or crustal contamination. The ankaramite, high-Mg basaltic andesite and high-Al andesite exhibit similar La/Sm ratios, $\epsilon_{\text{Nd}}(t)$ and ($^{87}\text{Sr}/^{86}\text{Sr}$)_i, indicating that the degree of mantle metasomatism may be comparable. Based on the variations of $\epsilon_{\text{Nd}}(t)$, ($^{87}\text{Sr}/^{86}\text{Sr}$)_i, La/Sm (Fig. 8a and b) and zircon Hf–O isotopes, all the rocks can be categorized into

three independent magmatic series: (1) boninite; (2) ankaramite–high-Mg basaltic andesite–high-Al andesite; (3) sanukite. The lithological assemblage of this region suggests an intra-oceanic arc setting, and thus crustal assimilation is likely to be insignificant during magma ascent *en route* to the surface. In addition, a high degree of crustal contamination can be precluded by (1) the small range of Hf–O isotope compositions and the presence of only a few xenocrystal zircons in the grain separate population from the studied rocks (Fig. 7) and (2) the lack of enclaves in the outcrops. Therefore, source metasomatism by subducted sediments of the mantle wedge is likely to be the dominant mechanism responsible for the chemical variation between the rock groups.

Petrogenesis of boninite

The boninite lavas, with low TiO₂ and Al₂O₃ and high contents of MgO and (Fe₂O₃)_T, do not show covariations between major or trace elements and SiO₂, as for other lavas, suggesting that the boninites are unlikely to be the evolved products of the parent magmas of the other lavas. Correlations between Si₂O–MgO, Si₂O–CaO and Cr–V suggest that the parental boninite magmas might have undergone pyroxene ($\pm\text{Ol}$)-dominated fractionation (Fig. 9).

Boninites may be produced by hydrous re-melting of refractory lherzolite, which is fluxed by slab-derived hydrous fluids or melts at high temperature and low pressure (spinel domain) (Green et al., 2004). In the Th/Yb–Nb/Yb proxy (Pearce, 2008) for recycled crustal components and selective Th and Nd addition, samples mainly plot above the mid-ocean ridge basalt (MORB)–OIB array (Fig. 10a). As shown in Fig. 10b and c, the boninite source was probably replenished by a fluid-like slab-derived component enriched in mobile elements (e.g. U and Ba), and relatively lacking in less fluid-mobile elements (e.g. Th and LREE). Although a role for a slab-derived fluid in the generation of the boninite is evident from Fig. 10b and c, the slight LREE and Th–Nd (Fig. 10a) enrichment cannot be explained by fluid-like subduction components alone, and also requires the presence of melt-like subduction components. Zircon $\delta^{18}\text{O}$ values of 6.57–7.61‰ from boninite (LJ15-01) are higher than that of primary mantle ($\delta^{18}\text{O} = 5.3 \pm 0.3\%$; Valley, 2003) (Fig. 11a). Similarly, the calculated whole-rock $\delta^{18}\text{O}$ values range from 6.23 to 8.49‰, higher than the $\delta^{18}\text{O}$ values of depleted mantle (5.7‰) and uncontaminated oceanic mantle plume sources ($\sim 6\%$) (Condie, 2001, and references therein). The sediment-derived fluids with elevated $\delta^{18}\text{O}$ values can be triggered by a contamination of the mantle with pelagic sediments ($\delta^{18}\text{O}$ values of c. 9–20‰) (Bindeman et al., 2005), which thus provide an appropriate candidate. Here, we employ a simple two end-member (peridotite plus oceanic sediments) mixing model for the Sr–Nd isotope compositions of the boninite samples, which restricts the amount of sediment-derived fluid in the

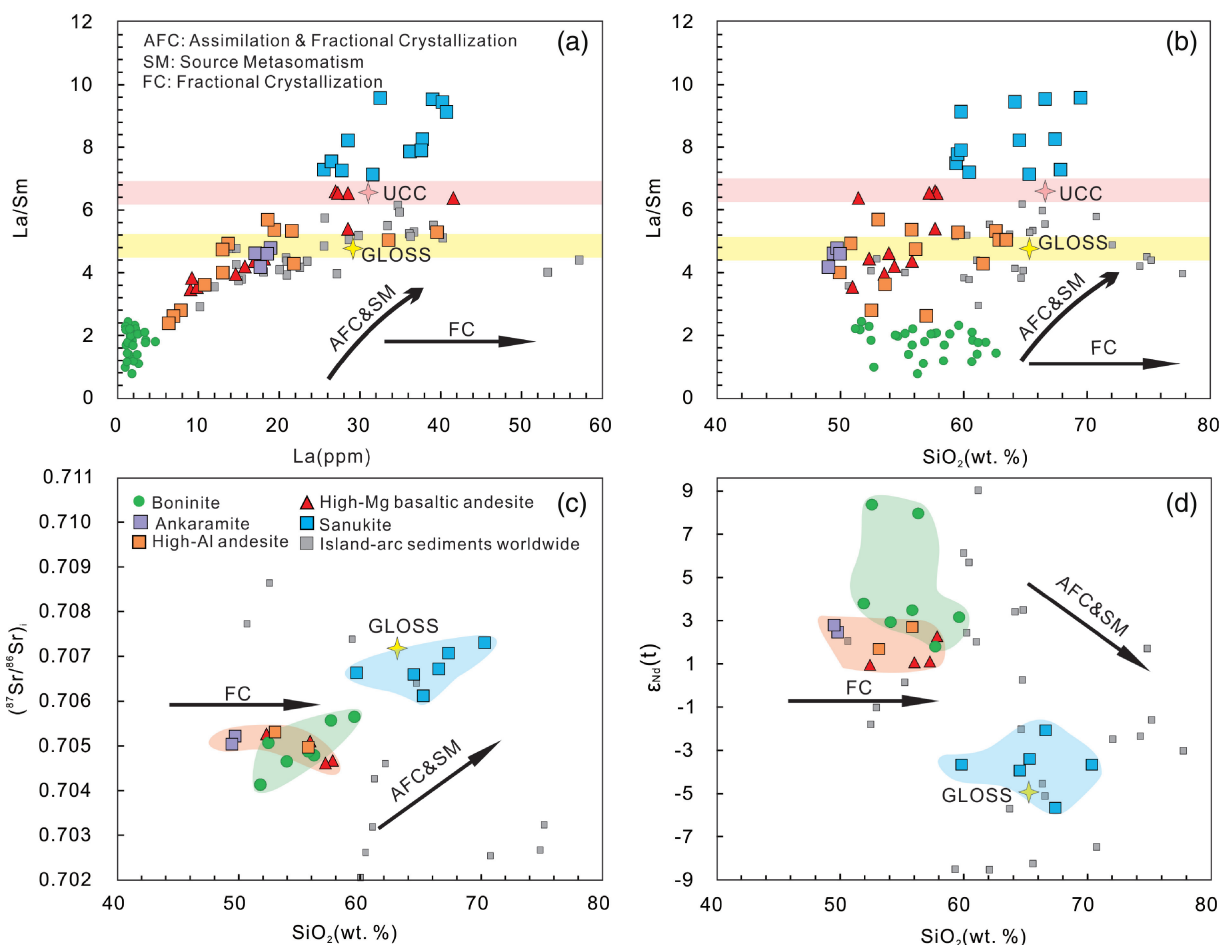


Fig. 8. (a) La/Sm vs La (ppm); (b) La/Sm vs SiO₂ (wt %); (c) (⁸⁷Sr/⁸⁶Sr)_i vs SiO₂ (wt %); (d) ε_{Nd}(t) vs SiO₂ (wt %). Data for UCC (upper continental crust) and GLOSS (Global Subducting Sediments) for comparison are respectively from Rudnick & Gao (2003) and Bebout (2014). The grey squares are average sediment data from different island arc systems (Bebout, 2014).

mantle source to less than 2% (Fig. 11b). We argue therefore that the involvement of silica-rich fluids derived from recycled pelagic sediments plays a crucial role in the formation of the boninite lavas.

Lines of evidence for the nature of depleted harzburgitic sources for boninites include the low contents of Al₂O₃ and high Cr# in Cr-spinel and the very low whole-rock HREE abundances. The average composition of our studied boninite samples is consistent with average boninite compositions worldwide (Fig. 12a). We use the depleted MORB mantle (DMM) from Workman & Hart (2005) as a model mantle source for the boninite. About 10–15% re-melting of DMM produces a good fit to the boninite glass data, except for a large discrepancy in Rb, Ba, Th, U and Sr owing to input from slab-derived components (Fig. 12a). Experimental studies indicate that progressive melting of fertile spinel lherzolite rapidly eliminates Cpx and gradually reduces the proportion of Opx at 10–20 kbar (Kelemen *et al.*, 1995). Primary Cpx is normally exhausted after 20–30% partial melting of lherzolite (e.g. Niu, 1997, 2004). Thus, we argue that the mantle source of boninite is a refractory, spinel-bearing, Cpx-poor lherzolite or harzburgite.

Formation of ankaramite–high-Mg basaltic andesite–high-Al andesite

The rock series of ankaramite, high-Mg basaltic andesite and high-Al andesite exhibits a large SiO₂ variation with relatively limited ranges of Sr–Nd isotope compositions (Fig. 8c and d). Also, the samples show a general linear trend between major and trace elements and SiO₂ (Fig. 9), suggesting that they may share a common magmatic lineage. The variation of Cpx compositions between ankaramite and high-Mg basaltic andesite is consistent with magma evolution. With the increase of SiO₂, the evolved samples show increases of TiO₂ and Al₂O₃ and decreases of MgO (Mg#), (Fe₂O₃)_T, CaO, Cr and Ni. Combined with the correlations between V and Cr, the parental magmas might have undergone Cpx-dominated fractionation from ankaramite to high-Mg basaltic andesite. High-Al basaltic lavas are volumetrically important lavas in many intra-oceanic island arcs and are often considered as derivative lavas (with plagioclase accumulation) of more primitive magmas containing 10–15% MgO, derived by partial melting of peridotite in the mantle wedge above the subducted slab (Crawford *et al.*, 1987). Importantly, the negative

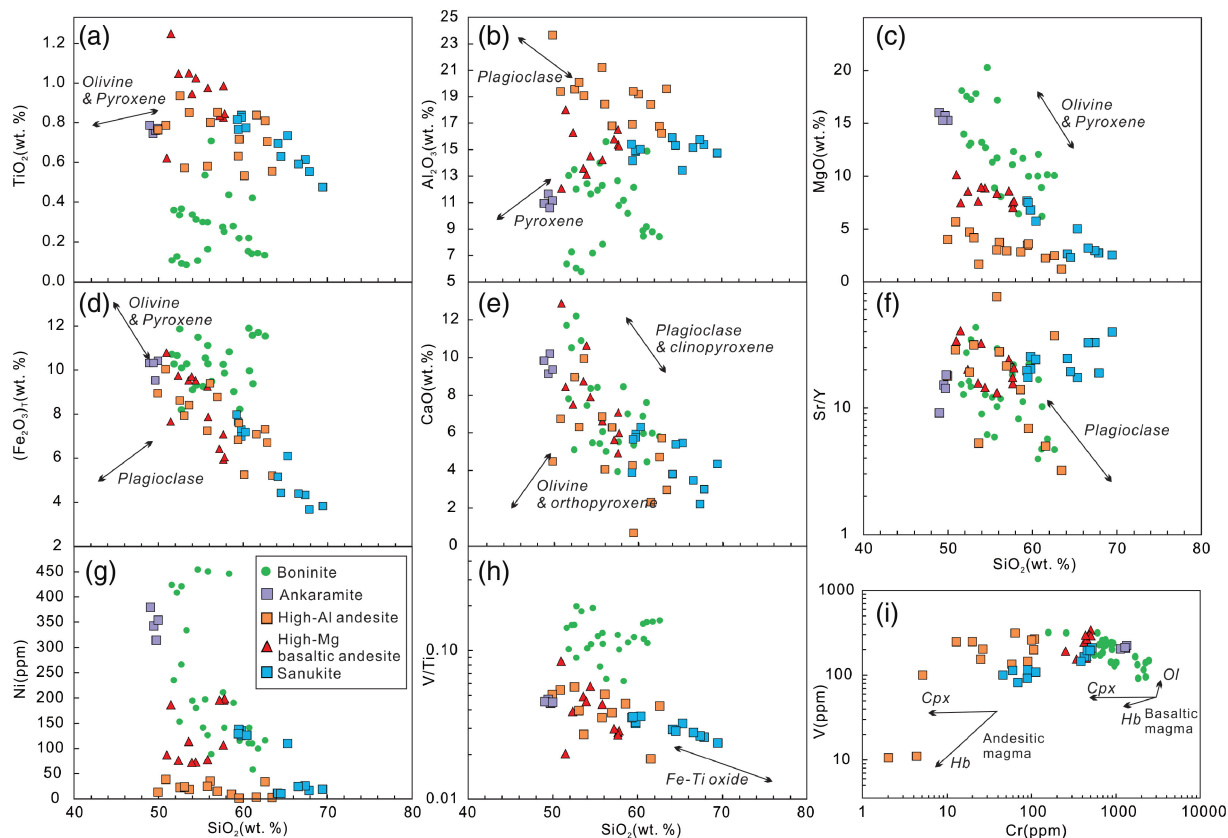


Fig. 9. Bulk-rock major and trace element (ratios) variation diagrams for island arc volcanic rocks from the Lajishan–Yongjing Terrane. The information used to deduce the vectors in these diagrams is from [Beier *et al.* \(2017\)](#) and [Greene *et al.* \(2006\)](#).

correlation between SiO_2 and MgO , $(\text{Fe}_2\text{O}_3)_T$, CaO , Al_2O_3 contents and Sr/Y , as well as the presence of both negative and positive Eu anomalies, indicates that plagioclase does become an important phase in the fractionating assemblage (Fig. 9). The decreases of MgO , Ni , $(\text{Fe}_2\text{O}_3)_T$ and CaO from ankaramite to high-Mg basaltic andesite and to high-Al andesite suggest a process from pyroxene-dominated fractionation to plagioclase accumulation (Fig. 9). Crystallization of V-rich, Fe–Ti oxides within the studied rocks is reflected by a trend of decreasing V/Ti and V versus SiO_2 (e.g. [Nielsen *et al.*, 1994](#)), and positive correlation between $(\text{Fe}_2\text{O}_3)_T$ and TiO_2 (not shown).

The ankaramite–high-Mg basaltic andesite–high-Al andesite series, as mentioned above, is likely to be an arc basaltic magmatic lineage with various degrees of Cpx fractional crystallization and Pl accumulation; the ankaramite lavas thus might be the nearest to the parental magma. Island arc ankaramites (nepheline-normative, CaO-rich and silica-poor) have been identified from many volcanic arcs worldwide (e.g. [Schiano *et al.*, 2000](#); [Green *et al.*, 2004](#)). The ankaramite samples, together with the high-Mg basaltic andesite, display enrichment of less fluid-mobile elements in Fig. 10a–c (e.g. Th and LREE), reflecting source input from subducted sediment-derived melts rather than fluids. Because Hf is also generally regarded as immobile in slab-derived fluids, a selective enrichment of Nd relative to Hf could be

expected, thereby leading to a decoupling of Hf–Nd compositions toward less radiogenic ϵ_{Nd} ([Pearce *et al.*, 1999](#)) and positive $\Delta\epsilon_{\text{Hf}}(t)$ values ([Vervoot *et al.*, 2011](#)). The positive $\Delta\epsilon_{\text{Hf}}(t)$ value of the high-Mg basaltic andesite (10-85) thus can be imparted through source contamination by zircon-barren pelagic sediments ([Chauvel *et al.*, 2008](#); [Choi *et al.*, 2013](#)) or selective melting of a mantle source containing high Lu/Hf minerals (e.g. [Bizimis *et al.*, 2003](#); [Choi & Mukasa, 2012](#)), the latter of which cannot lead to the conspicuous elevation of O isotopic compositions ([Wang *et al.*, 2014](#)). Given that the zircons from the high-Al andesite sample have elevated $\delta^{18}\text{O}$ values (Fig. 11a) relative to primary mantle ($\delta^{18}\text{O} = 5.3 \pm 0.3\text{‰}$; [Valley, 2003](#)), we argue that the positive $\Delta\epsilon_{\text{Hf}}(t)$ value of the high-Mg basaltic andesite (10-85) may be due to source contamination by zircon-barren pelagic sediments. Figure 11 illustrates the results of Sr–Nd–Hf mixing calculations in the case of slab dehydration and slab melting, respectively ([Hanyu *et al.*, 2006](#)). The Sr–Nd data for ankaramite, high-Mg basaltic andesite and high-Al samples are well accounted for by the addition of ~2–4% of sediment-derived melt or fluid into the mantle wedge, consistent with the results of the Hf–Nd mixing calculation (1–3%) for high-Mg basaltic andesite (Fig. 11b and c).

The primitive features of the ankaramites, including high Mg#, Cr and Ni contents and Cr-rich spinel, are shared with other primitive arc magmas such as

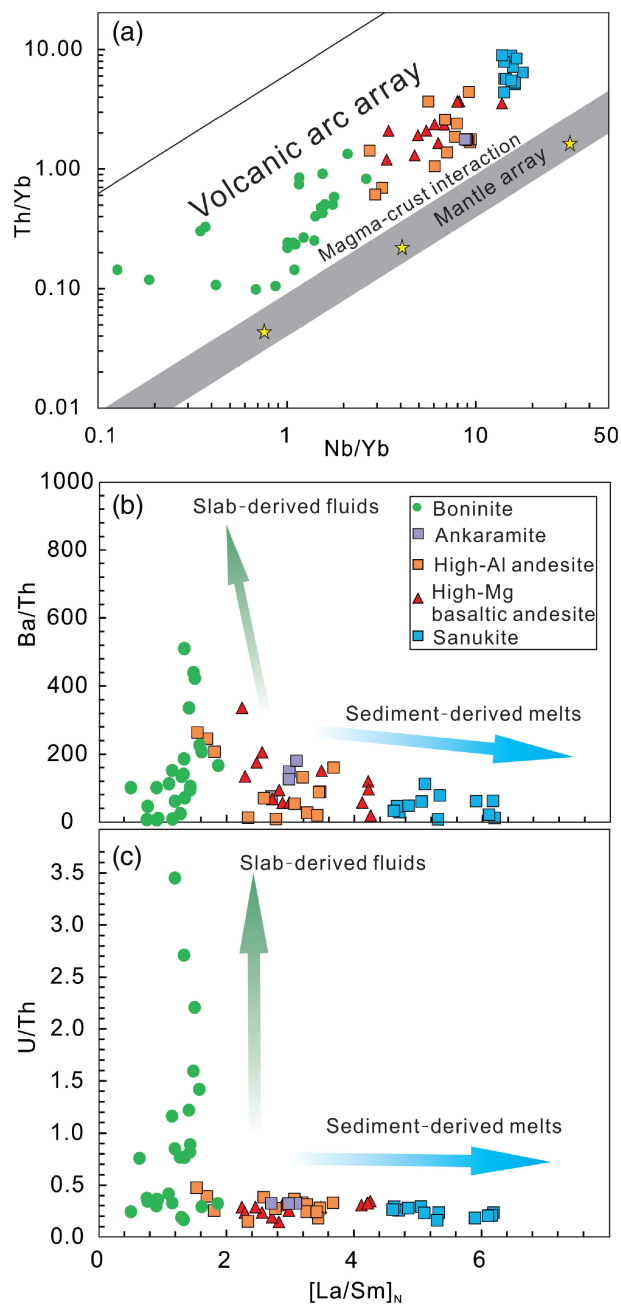


Fig. 10. Variation of (a) Th/Yb vs Nb/Yb (Pearce, 2008), (b) Ba/Th and (c) U/Th vs chondrite-normalized La/Sm.

boninites [e.g. Fo (Ol) >90; Cr# (Sp) >70; Crawford *et al.*, 1989]. Previous experimental work has shown that the primitive island arc ankaramitic lavas could be segregated from residual harzburgite at 1.5 GPa, ~1320–1350°C, fluxed by dolomitic carbonatite melts (C–H–O melts) (Green *et al.*, 2004); Only high-pressure melts (above 1.5–1.8 GPa) from peridotite are silica-undersaturated (e.g. Till *et al.*, 2012). However, others have argued against this scenario because the high-pressure experimental melts have insufficiently high CaO/Al₂O₃ ratios and nepheline-normative contents, as well as the presence of residual garnet in the source, which contradicts the observation of ankaramitic melt

inclusions with high CaO/Al₂O₃ ratios and flat REE spectra (Elburg *et al.*, 2007; Sorbadere *et al.*, 2013a). Therefore, another mechanism is required for the genesis of the ankaramitic melt inclusions that involves partial melting of amphibole-bearing, Cpx-rich cumulative pyroxenite lithologies at lower crustal or shallow upper mantle pressures (e.g. Schiano *et al.*, 2000; Médard *et al.*, 2006; Sorbadere *et al.*, 2013a). The high temperatures, however, needed to form nepheline-normative arc melt inclusions (up to 1300°C; Schiano *et al.*, 2000; Sorbadere *et al.*, 2013a) are difficult to reconcile with arc crust melting, which argues against the melting of lower crustal cumulates as directly responsible for the common pyroxenitic signature of primitive arc magmas. Thus, both the peridotite melts and clinopyroxenite melts in the mantle wedge must be important. Recent experimental results also argue for the involvement of a heterogeneous hydrous mantle source composed of lherzolite mixed with amphibole-bearing clinopyroxenite as a more realistic model for the formation of arc ankaramitic melt inclusions (Sorbadere *et al.*, 2013b).

Oscillatory zoning and variation of Mg# in Cpx, and compositional changes of the Cr-spinel included in Cpx phenocrysts and in the matrix, indicate several stages of disequilibrium melt evolution. Thus, it is reasonable to use the high Mg# Cpx cores to back-calculate the parental melts of the ankaramite. The back-calculated melt concentrations of trace element for the Cpx cores with the highest Mg# are used for consideration as the parental magmas of the ankaramite, and are illustrated in Fig. 12b. The calculated parental magmas have low REE contents with slightly right inclined HREE patterns (Fig. 12b), suggesting their derivation from the source region with garnet as a residual phase. Thermobarometry calculations using the Cpx compositions result in estimates of the potential temperature (T_p) of the mantle source ranging from 1267 to 1316°C (1296°C on average) and equilibration pressures of 11.6–20.0 kbar (16.6 kbar on average), using the equation of Putirka (2008). We propose that this rock series is likely to be derived from a heterogeneous, hydrous, garnet-bearing mantle source composed of lherzolite and clinopyroxenite.

Formation of sanukite

The sanukite lavas have nearly constant Al₂O₃ and Sr/Y ratios over a wide range of SiO₂ contents. The absence of an obvious Eu negative anomaly suggests insignificant fractional crystallization of plagioclase. However, the decreased MgO, (Fe₂O₃)_T, and CaO with increasing SiO₂, together with the correlations between Cr–Ni and Cr–V, are consistent with the fractional crystallization of pyroxene and hornblende (Fig. 9).

Sanukite and the equivalent of sanukitoids found in the Setouchi volcanic belt, SW Japan, are one type of the known high-Mg andesites (Mg# >64, Tatsumi, 2006). They are likely to represent little differentiated,

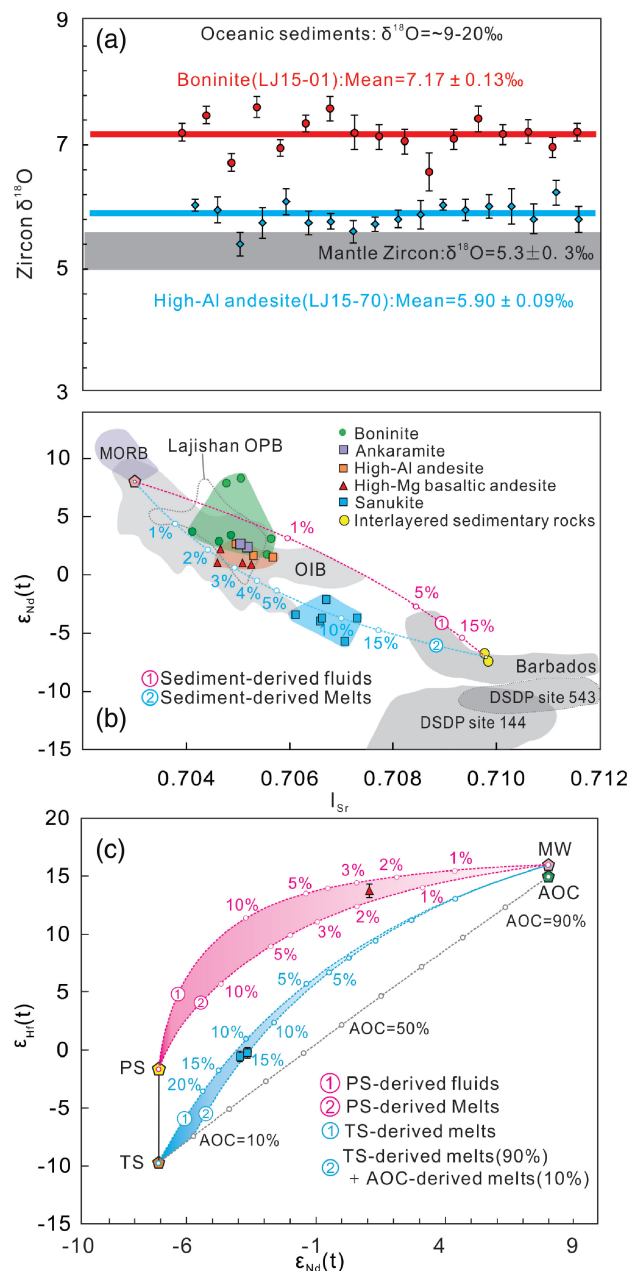


Fig. 11. (a) Zircon O isotopic compositions for island arc volcanic rocks from the Lajishan–Yongjing Terrane. Data sources: mantle $\delta^{18}\text{O}$ value (5.3 ± 0.3 ‰) from Valley (2003); pelagic sediments and terrigenous sediments ($\delta^{18}\text{O} = 9$ – 20 ‰) from Bindeman *et al.* (2005), Chauvel *et al.* (2008), and Vervoort *et al.* (2011). (b) Sr–Nd isotopic compositions for the Lajishan–Yongjing volcanic rocks showing the two-component mixing models. Data sources: fields labelled MORB and sediments from Barbados, and Deep Sea Drilling Project (DSDP) sites 144 and 543 are from Bezard *et al.* (2015) and reference therein. The OIB data are from White (2010). The Lajishan oceanic plateau basalts (OPB) data without the altered samples are from Zhang *et al.* (2017). (c) Nd–Hf isotopic compositions of the Lajishan–Yongjing volcanic rocks showing the mixing model between the mantle wedge (MW), subducted altered oceanic crust (AOC) and oceanic sediments, assuming slab dehydration and melting. The dashed mixing trajectories are between the mantle wedge and these different fluxing agents. The pink area is restricted by the mixing trajectories of zircon-barren pelagic sediment-derived fluids and melts. The blue area is restricted by the mixing trajectories of terrigenous sediment-

near-primitive andesite magmas generated in the presence of sufficient H_2O by equilibrium reaction of a hot mantle peridotite with a silicic melt derived from partial melting of a subducting sediments and/or the oceanic slab (e.g. Yogodzinski *et al.*, 1994; Shimoda *et al.*, 1998). As mentioned above, the studied sanukite lavas are similar in major and trace element composition to Japanese sanukite or sanukitoids. As shown in Fig. 10a–c, the addition of sediment-derived silicic melts rather than aqueous fluids is required to explain the petrogenesis of the sanukite samples. Furthermore, the sanukite samples tend to have more radiogenic Sr–Nd–Hf isotopic compositions than other lavas in this study, suggesting a higher degree of source mixing with a metasomatic agent. The two end-member mixing model for Sr–Nd isotopes for the sanukite samples restricts the amount of additional sediment-derived melt in the mantle source to 8–12% (Fig. 11b). The Hf–Nd isotopic data are consistent with the Sr–Nd isotope mixing model between sediment-derived melt and the mantle wedge, requiring 10–15% addition of metasomatic melt comprising a 9:1 mixture of sediments versus altered oceanic crust (Fig. 11c). Compared with adakites, the sanukite samples have transitional Sr/Y ratios of 17.5–39.9 (Fig. 9f), intermediate between adakites and typical arc magmas, implying that the subducted slab or sediments may have melted at depths shallower than the garnet stability field.

The heterogeneity of the mantle source: depleted versus plume-enriched

Primitive arc magmas (i.e. the boninites, ankaramites and sanukites of this study) are in principle ideal probes of sub-arc mantle sources (Falloon & Danyushevsky, 2000; Green *et al.*, 2004; Mitchell & Grove, 2015; Bénard *et al.*, 2016). Although the Lajishan–Yongjing volcanic rocks exhibit large variations in major and trace element compositions, most primitive samples have distinctive geochemical signatures, including high MgO contents with corresponding Mg# values, Cr and Ni concentrations, implying their derivation from partial melting of mantle source(s). Elemental and isotopic variations show the heterogeneity of the mantle sources among the different rock series. The boninite lavas are derived from a depleted mantle source

Fig. 11. Continued

derived melts and 90% terrigenous sediment-derived melts + 10% AOC-derived melts. Numbers along the pink and blue mixing trajectories are the amount of the crust-derived input and numbers along the gray lines are the proportion of the AOC component. The end-member compositions are from Hanyu *et al.* (2006) and are listed in Supplementary Data Appendix Table 6. The I_{Sr} and $\epsilon_{\text{Nd}}(t)$ values of sediments are from the measured interlayered sedimentary rocks between the Lajishan–Yongjing volcanic rocks, and the $\epsilon_{\text{Hf}}(t)$ values for the pelagic clay sediments [PS: $\epsilon_{\text{Hf}}(t) = 0.99\epsilon_{\text{Nd}}(t) + 5.34$] and terrigenous sediments [TS: $\epsilon_{\text{Hf}}(t) = 1.55\epsilon_{\text{Nd}}(t) + 1.21$] are calculated using the sediment arrays recommended by Vervoort *et al.* (2011) and Wang *et al.* (2014), respectively. Symbols are larger than the maximum analytical error isotope on the isotope data, except where shown.

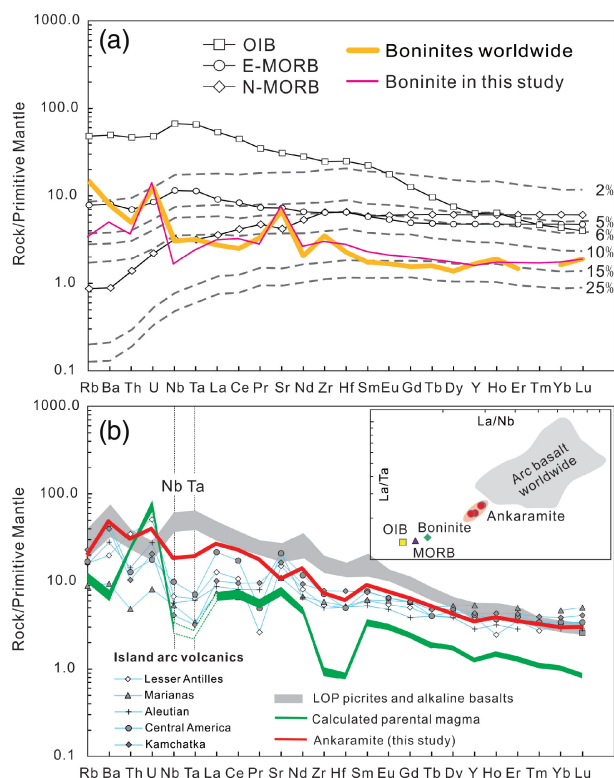


Fig. 12. Primitive mantle (PM)-normalized trace element patterns for the average compositions of (a) boninite, (b) primitive ankaramite and the calculated parental magmas of Cpx-phyric basaltic andesite in Lajishan–Yongjing Terrane. The average compositions of boninite are from near-primitive samples (15LJ-13, 16LJ-07, -09 and -15) with a high Mg# of 74–80; the average compositions of ankaramite are from sample 13QLS-68-72 (Mg# = 77–79). In (a) grey dashed lines represent the liquids produced by aggregated fractional melting of a DMM source and the numbers represent the melting degree of mantle (Workman & Hart, 2005). Data for comparison are: OIB, enriched (E)-MORB, normal (N)-MORB (Sun & McDonough, 1989) and the average composition of boninites worldwide (Kelemen *et al.*, 2003). (b) The calculated parental magmas are based on the trace element composition of a high Mg# Cpx phenocryst from Cpx-phyric basaltic andesite sample 13QLS-124; the amounts of Cpx phenocrysts are assumed to range from 0 to 40 wt %; clinopyroxene/melt partition coefficients (K_D) and their sources are listed in Supplementary Data Appendix Table 3. Data shown for comparison are island arc volcanic rocks (Kelemen *et al.*, 2003), and the LYO (Lajishan–Yongjing Ophiolite) picrites and alkali basalts (Zhang *et al.*, 2017).

composed of refractory, spinel-bearing, Cpx-poor lherzolite or harzburgite. In contrast, the ankaramite lavas are derived from a heterogeneous garnet-bearing, mantle lherzolite mixed with amphibole-bearing clinopyroxenite.

Pyroxenites have been widely described either from arc environments or plume-enriched intraplate mantle, and are interpreted either as lower crustal Cpx-rich cumulates from the deep arc crust or as metasomatic rocks in the mantle induced by metasomatism from slab-derived components or plume-related components (e.g. Ishikawa *et al.*, 2004; Sobolev *et al.*, 2005; Berly *et al.*, 2006; Greene *et al.*, 2006). Specifically, an OIB-

type enriched mantle source that had melt components incorporated into it before the onset of subduction would constitute a secondary pyroxenitic source (Sobolev *et al.*, 2005), which is consistent with the observed coarse-grained pyroxenite in the lower part of the Lajishan–Yongjing lithological sequence. Such situations are documented for the mantle sources beneath the Ontong Java Plateau (Ishikawa *et al.*, 2004) and Hawaii (Sobolev *et al.*, 2005). Amphibole-clinopyroxenite heterogeneities in the mantle wedge could originate by density-driven delamination of lower crustal cumulates consisting of clinopyroxene + amphibole \pm olivine (Sorbadere *et al.*, 2013b), and there is geochemical evidence that the clinopyroxenophytic ankaramite–basaltic andesites are derived from the same or similar plume-enriched mantle sources in the adjacent Lajishan–Yongjing Oceanic Plateau (Zhang *et al.*, 2017). The direct evidence is that the ankaramites plot between the alkali basalt and picrite samples from the Lajishan–Yongjing Ophiolite and show similar trace element patterns except for Nb–Ta depletion and U enrichment; their La/Nb and La/Ta ratios show transitional values between OIB–MORB and normal intra-oceanic arc basalts worldwide (Fig. 12b). The high TiO₂ contents of both Cr-spinel inclusions and Cpx (Figs 5a and 6a), relative to those from normal fore-arc peridotites and island arc volcanic rocks, suggest that the primitive magmas are derived from a Ti-rich mantle source. In addition, the positive correlation between the TiO₂ and Al₂O₃ contents of Cr-spinel from boninite (15LJ-12) and enriched-boninite (15LJ-15) to ankaramite (13QLS-68 and -72) form an obvious trend toward the Lajishan–Yongjing Oceanic Plateau (Fig. 5a), showing an increasing influence of a plume-enriched mantle source. In contrast, the decreased Cr# of chrome spinel from those samples suggests a decreased degree of partial melting of the mantle source. In terms of whole-rock Sr–Nd isotopic compositions, the $\epsilon_{Nd}(t)$ values of ankaramite (and the derivative high-Mg basaltic andesite and high-Al andesite lavas) are slightly lower than those of boninite lavas (Fig. 11b), which may reflect an enriched mantle source prior to or during the contamination by the slab-derived component.

In conclusion, we have identified three primitive melt compositions from the same arc—boninite, ankaramite, and sanukite—all of which were generated in roughly the same time interval. The diversity of the studied primitive rocks can be attributed to heterogeneous mantle sources and variable degrees of mantle metasomatism by sediment-derived hydrous fluids or silicic melts. Partial melting of the subducted oceanic crust and its overlying oceanic sediments would produce the aqueous fluids or silicic melts, which are respectively enriched in fluid-mobile incompatible elements solely (e.g. U, Ba) or with less fluid-mobile incompatible elements (e.g. Th, LREE), with various Sr–Nd–Hf–O isotope compositions. Different amounts of slab-derived components with different proportions of

fluid versus melt would be incorporated into, and then react with, the overlying mantle wedge. Owing to the plume-related mantle metasomatism before the onset of subduction, the sub-arc mantle source(s) in the SQAB is likely to be spatially compositionally heterogeneous, and thus capable of producing various primitive arc magmas. Subsequently, the primitive arc magmas are likely to have undergone a secondary AFC process during their ascent *en route* to the surface.

Tectonic implications

The geodynamic setting of the intra-oceanic island arc: interaction between oceanic arc and oceanic plateaux

Accretion of an oceanic plateau to a continental margin would require that it was transferred from an oceanic to a continental setting by subduction-zone tectonic processes (Coffin & Eldholm, 2001). Several different tectonic scenarios, ranging from an entirely subducted model, through a partly preserved model to a totally accreted model, have been proposed for the fate of oceanic plateaux on reaching subduction zones (e.g. Saunders *et al.*, 1996; Pettersen *et al.*, 1999; Kerr *et al.*, 2000). The western Pacific Ocean region provides abundant examples of the interaction between oceanic arcs and oceanic plateaux; the Cenozoic Circum-Pacific oceanic plateaux are now located in intraplate settings and trapped settings, where the plateaux are now trapped in an intercontinental or continental margin setting by outward subduction (Mann & Taira, 2004; Song *et al.*,

2017). Thus, oceanic plateaux, owing to their widespread distribution on the seafloor and continental-like crustal thicknesses, might be expected to behave more like continents upon reaching subduction zones, and thus accrete rather than subduct (Nur & Ben-Avraham, 1982; Niu *et al.*, 2017). Transference and polarity reversal are distinguished as two sub-classes of the induced nucleation model in which the newly formed subduction zone was respectively moved to the outboard of the failed ones and behind the magmatic arc (Stern 2004, 2010). Accordingly, an oceanic plateau is an important candidate for the formation of an intra-oceanic island arc and can be preserved as fragments (Niu *et al.*, 2003, 2017).

The geodynamic setting of the Lajishan–Yongjing Terrane of the Qi–Qin Accretionary Belt, where an extensive ophiolite fragment, an island arc volcanic complex and arc-related plutonism are juxtaposed, has long been the subject of debate. Recent investigations suggest that this accretionary belt comprises two distinct components: (1) a Cambrian (>500 Ma) ophiolite complex with picrites and OIB-type lavas that represent an oceanic plateau (Hou *et al.*, 2005; Song *et al.*, 2017; Zhang *et al.*, 2017; Yang *et al.*, 2018); (2) an Ordovician (<470 Ma) island arc complex (this study). As shown in Fig. 13, the Lajishan–Yongjing ophiolites were the products of a Cambrian mantle plume that formed an oceanic plateau in the Proto-Tethys Ocean, and were accreted as an ophiolitic component in the accretionary belt (Song *et al.*, 2017; Zhang *et al.*, 2017). Subsequently, as argued above, the Lajishan–Yongjing arc volcanic

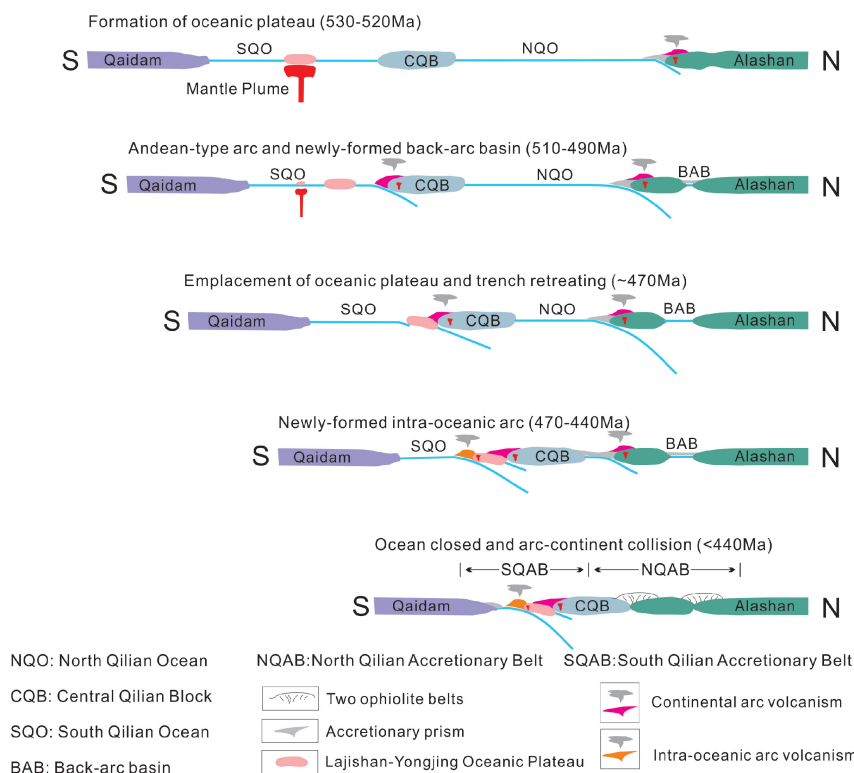


Fig. 13. Schematic illustrations showing the tectonic evolution of the South Qilian Accretionary Belt in the Qilian Orogen.

system could be considered as a newly formed island arc system erupting along the oceanic plateau margins in response to the collision between the oceanic plateau and the pre-existing trench or continental margin. *In situ* zircon U–Pb data reveal that the Lajishan–Yongjing arc volcanic system formed at ~460–440 Ma, much younger than the ophiolite fragments, and thus constrain the ages of volcanism and intra-oceanic subduction of the South Qilian Ocean.

Tectonic evolution from continental arc to intra-oceanic arc in North Qilian and South Qilian

The mechanisms of evolution from continental arc to intra-oceanic arc include (1) trench retreat, with the corresponding extension of the overriding plate and subsequent opening of a back-arc basin resulting from slab roll-back, and (2) trench jamming related to the incorporation of an oceanic plateau or a microcontinent. In Fig. 13, based on the studied rock assemblages, the NQAB is considered to be an Andean-type active continental margin with the development of a back-arc basin in the Early Paleozoic era, recording the subduction history of the Qilian Ocean beneath the Alax Block (Wu *et al.*, 1993; Song *et al.*, 2006, 2009, 2013; Zhang *et al.*, 2007). The development of a back-arc basin in the NQAB (~510–450 Ma) is due to the separation of continental fragments as a result of slab roll-back at the continental margin (Xia *et al.*, 2012; Song *et al.*, 2013). In contrast, the SQAB is recognized as an Early Paleozoic subduction accretionary belt, formed by accretion of plume-type ophiolite fragments (Zhang *et al.*, 2017) with outboard intra-oceanic arc volcanism as well as intrusion of arc-related plutons at c. 460–440 Ma. The accretion of oceanic plateaux and trench jamming are the main reason for the cessation of the existing subduction zone and initiation of a new intra-oceanic island arc. Therefore, in the Early Paleozoic subduction history of the Qilian Ocean, evolution from continental margin to oceanic island arc can be attributed to trench retreat in the NQAB and trench jamming in the SQAB, respectively.

CONCLUSIONS

Five distinct rock lineages have been recorded in the volcanic sequence in the Lajishan–Yongjing Terrane: boninite, ankaramite, high-Mg basaltic andesite, high-Al andesite and sanukite. The assemblage shows arc-like trace element distribution patterns and suggests an Izu–Bonin–Mariana-type oceanic island arc in the Early Paleozoic era. The enriched Sr–Nd and decoupled Hf–Nd isotopic systems, as well as anomalous zircon $\delta^{18}\text{O}$ values, suggest the incorporation of subducted oceanic sediments into the mantle source of the parental magmas. The boninites were derived from refractory, Cpx-poor spinel lherzolite or harzburgite. The ankaramite and high-Mg basaltic andesite were probably derived from an OIB-enriched, garnet-bearing, pyroxenitic–

peridotitic mixed mantle source; the high-Al andesites are evolved magmas after fractionation of Cpx. The sanukites could have been generated by the equilibrium reaction of mantle peridotite with a silicic melt derived from partial melting of subducted sediments. Large compositional variations in the volcanic sequence from the same arc over such a short time interval show that oceanic arc magmas derived from a significantly heterogeneous mantle source simultaneously, accompanied by a secondary AFC process during their ascent *en route* to the surface.

The generation of the arc volcanic sequence in the Lajishan–Yongjing accretionary belt is a response to the collision between the Lajishan–Yongjing ocean plateau and the pre-existing trench or continental margin. Zircon ages of ~440–460 Ma constrain the age of volcanism, as well as the intra-oceanic subduction of the Qilian Ocean. In the early Paleozoic subduction history of the Qilian Ocean, two processes can be responsible for the evolution from continental margin to oceanic island arc: trench retreat in the NQAB and trench jamming in the SQAB, respectively.

ACKNOWLEDGEMENTS

The authors wish to thank H. Y. Zhang for helping with the whole-rock analyses, G. B. Zhang and W. P. Zhu for helping with Sr–Nd isotope analyses, J. Li and Y. G. Li for helping with zircon SIMS and LA-ICP-MS U–Pb dating analysis and zircon Hf–O isotope analysis, and X. L. Li and H. Y. Zhang for helping with mineral analysis. The authors are grateful to Editor John Gamble, Rod Sewell and one anonymous reviewer for their detailed and constructive peer-review comments, which greatly improved the quality of this paper.

FUNDING

This study was supported by the National Natural Science Foundation of China (Grant 41572040) and the Major State Basic Research Development Program (2015CB856105).

SUPPLEMENTARY DATA

Supplementary data for this paper are available at *Journal of Petrology* online.

REFERENCES

- Andersen, T. (2002). Correction of common lead in U–Pb analyses that do not report ^{204}Pb . *Chemical Geology* **192**, 59–79.
- Barsdell, M. & Berry, R. F. (1990). Origin and evolution of primitive island-arc ankaramites from Western Epi, Vanuatu. *Journal of Petrology* **31**, 747–777.
- Bebout, G. E. (2014). Chemical and isotopic cycling in subduction zones. In: Turekian, K. K. & Holland, H. D. (eds) *Treatise on Geochemistry, The Crust*, 2nd edn. Amsterdam: Elsevier, pp. 703–747.

- Beier, C., Haase, K. M., Brandl, P. A. & Krumm, S. H. (2017). Primitive andesites from the taupo volcanic zone formed by magma mixing. *Contributions to Mineralogy and Petrology* **172**, 33.
- Bénard, A., Nebel, O., Ionov, D. A., Arculus, R. J., Shimizu, N. & Métrich, N. (2016). Primary silica-rich picrite and high-Ca boninite melt inclusions in pyroxenite veins from the Kamchatka sub-arc mantle. *Journal of Petrology* **57**, 1955–1982.
- Berly, T. J., Hermann, J., Arculus, R. J. & Lapiere, H. (2006). Supra-subduction zone pyroxenites from San Jorge and Santa Isabel (Solomon Islands). *Journal of Petrology* **47**, 1531–1555.
- Bezard, R., Turner, S., Davidson, J. P., Macpherson, C. G. & Lindsay, J. M. (2015). Seeing through the effects of crustal assimilation to assess the source composition beneath the Southern Lesser Antilles Arc. *Journal of Petrology* **56**, 815–844.
- Bindeman, I. N., Eiler, J. M., Yagodinski, G. M., Tatsumi, Y., Stern, C. R., Grove, T. L., Portnyagin, M., Hoernle, K. & Danyushevsky, L. V. (2005). Oxygen isotope evidence for slab melting in modern and ancient subduction zones. *Earth and Planetary Science Letters* **235**, 480–496.
- Bizimis, M., Salters, V. J. M. & Dawson, J. B. (2003). The brevity of carbonatite sources in the mantle: evidence from Hf isotopes. *Contributions to Mineralogy and Petrology* **145**, 281–300.
- Blichert-Toft, J. & Albarède, F. (1997). The Lu–Hf isotope geochemistry of chondrites and the evolution of the mantle–crust system. *Earth and Planetary Science Letters* **148**, 243–258.
- Cao, Y., Song, S. G., Su, L., Jung, H. & Niu, Y. L. (2016). Highly refractory peridotites in Songshugou, Qinling orogen: insights into partial melting and melt/fluid–rock reactions in forearc mantle. *Lithos* **252–253**, 234–254.
- Cawood, P. A., Kröner, A., Collins, W. J., Kusky, T. M., Mooney, W. D. & Windley, B. F. (2009). Accretionary orogens through Earth history. In: Cawood, P. A. & Kröner, A. (eds) *Earth Accretionary Systems in Space and Time*. Geological Society, London, Special Publications **318**, 1–36.
- Chauvel, C., Lewin, E., Carpentier, M., Arndt, N. T. & Marini, J. C. (2008). Role of recycled oceanic basalt and sediment in generating the Hf–Nd mantle array. *Nature Geoscience* **1**, 64–67.
- Choi, H. O., Choi, S. H., Lee, D. C. & Kang, H. C. (2013). Geochemical evolution of basaltic volcanism within the Tertiary basins of southeastern Korea and the opening of the East Sea (Sea of Japan). *Journal of Volcanology and Geothermal Research* **249**, 109–122.
- Choi, S. H. & Mukasa, S. B. (2012). Lu–Hf and Sm–Nd isotope systematics of Korean spinel peridotites: a case for metasomatically induced Nd–Hf decoupling. *Lithos* **154**, 263–276.
- Chu, N. C., Taylor, R. N., Chavagnac, V., Nesbitt, R. W., Boella, R. M., Milton, J. A., Germain, C. R., Bayon, G. & Burton, K. (2002). Hf isotope ratio analysis using multi-collector inductively coupled plasma mass spectrometry: an evaluation of isobaric interference corrections. *Journal of Analytical Atomic Spectrometry* **17**, 1567–1574.
- Coffin, M. & Eldholm, O. (2001). Large igneous provinces: progenitors of some ophiolites? In: Ernst, R. & Buchan, K. (eds) *Mantle Plumes: Their Identification through Time*. Geological Society of America, *Special Papers* **352**, 59–70.
- Condie, K. C. (2001). *Mantle Plumes and Their Record in Earth History*. Cambridge: Cambridge University Press, 306 pp.
- Condie, K. C. (2014). Growth of continental crust: a balance between preservation and recycling. *Mineralogical Magazine* **78**, 623–638.
- Crawford, A. J., Falloon, T. J. & Eggins, S. (1987). The origin of island arc high-alumina basalts. *Contributions to Mineralogy and Petrology* **97**, 417–430.
- Crawford, A. J., Falloon, T. J. & Green, D. H. (1989). Classification, petrogenesis and tectonic setting of boninites. In: Crawford, A. J. (ed.) *Boninites and Related Rocks*. London: Unwin Hyman, pp. 1–49.
- Dick, H. J. B. & Bullen, T. (1984). Chromian spinel as a petrogenetic indicator in abyssal and alpine-type peridotites and spatially associated lavas. *Contributions to Mineralogy and Petrology* **86**, 54–76.
- Elburg, M. A., Kamenetsky, V. S., Foden, J. D. & Sobolev, A. (2007). The origin of medium-K ankaramitic arc magmas from Lombok (Sunda arc, Indonesia): mineral and melt inclusion evidence. *Chemical Geology* **240**, 260–279.
- Falloon, T. J. & Danyushevsky, L. V. (2000). Melting of refractory mantle at 1.5, 2.0 and 2.5 GPa under H₂O-undersaturated conditions: implications for the petrogenesis of high-Ca boninites and the influence of subduction components on mantle melting. *Journal of Petrology* **41**, 257–283.
- Fu, C. L., Yan, Z., Guo, X. Q., Niu, M. L., Xia, W. J., Wang, Z. Q. & Li, J. L. (2014). Geochemistry and SHRIMP zircon U–Pb age of diabases in the Lajishankou ophiolitic mélange, South Qilian terrane. *Acta Petrologica Sinica* **30**, 1695–1706 (in Chinese with English abstract).
- Gehrels, G. E., Yin, A. & Wang, X. F. (2003). Detrital-zircon geochronology of the northeastern Tibetan plateau. *Geological Society of America Bulletin* **115**, 881–896.
- Gill, J. B. (1981). *Orogenic andesites and plate tectonics*. Berlin: Springer, pp. 1–358.
- Green, D. H., Schmidt, M. W. & Hibberson, W. O. (2004). Island-arc ankaramites: primitive melts from fluxed refractory Iherzolitic mantle. *Journal of Petrology* **45**, 391–403.
- Greene, A. R., Debari, S. M., Kelemen, P. B., Blusztajn, J. & Clift, P. D. (2006). A detailed geochemical study of island arc crust: the Talkeetna arc section, South–Central Alaska. *Journal of Petrology* **47**, 1051–1093.
- Griffin, W. L., Pearson, N. J., Belousova, E., Jackson, S. E., van Acherbergh, E., O’Reilly, S. Y. & Shee, S. R. (2000). The Hf isotope composition of cratonic mantle: LA-MC-ICP-MS analysis of zircon megacrysts in kimberlites. *Geochimica et Cosmochimica Acta* **64**, 133–147.
- Griffin, W. L., Belousova, E. A., Shee, S. R., Pearson, N. J. & O’Reilly, S. Y. (2004). Archean crustal evolution in the northern Yilgarn Craton: U–Pb and Hf-isotope evidence from detrital zircons. *Precambrian Research* **131**, 231–282.
- Hanyu, T., Tatsumi, Y., Nakai, S. I., Chang, Q., Miyazaki, T., Sato, K., Tani, K., Shibata, T. & Yoshida, T. (2006). Contribution of slab melting and slab dehydration to magmatism in the NE Japan arc for the last 25 Myr: constraints from geochemistry. *Geochemistry, Geophysics, Geosystems* **7**, 1–29.
- Hou, K. J., Li, Y. H., Zou, T. R., Qu, X. M., Shi, Y. R. & Xie, G. Q. (2007). Laser ablation-MC-ICP-MS technique for Hf isotope microanalysis of zircon and its geological applications. *Acta Petrologica Sinica* **23**, 2595–2604 (in Chinese with English abstract).
- Hou, Q. Y., Zhao, Z. D., Zhang, H. F., Zhang, B. R., Zhang, L. & Chen, Y. L. (2005). Discussion on the tectonic affinity of ancient oceanic mantle in Western Qinling–Songpan continental tectonic node China: from elemental and Sr–Nd–Pb isotopic evidences. *Acta Petrologica Sinica* **22**, 2901–2909 (in Chinese with English abstract).
- Iizuka, T. & Hirata, T. (2005). Improvements of precision and accuracy in *in situ* Hf isotope microanalysis of zircon using the laser ablation-MC-ICPMS technique. *Chemical Geology* **220**, 121–137.

- Ishikawa, A., Maruyama, S. & Komiya, T. (2004). Layered lithospheric mantle beneath the Ontong Java Plateau: implications from xenoliths in alnöite, Malaita, Solomon Islands. *Journal of Petrology* **45**, 2011–2044.
- Jacobsen, S. B. & Wasserburg, G. J. (1980). Sm–Nd isotopic evolution of chondrites. *Earth and Planetary Science Letters* **50**, 139–155.
- Kamenetsky, V. S., Crawford, A. J. & Meffre, S. (2001). Factors controlling chemistry of magmatic spinel: an empirical study of associated olivine, Cr-spinel and melt inclusions from primitive rocks. *Journal of Petrology* **42**, 655–671.
- Kelemen, P. B., Shimizu, N. & Salters, V. M. (1995). Extraction of mid-ocean-ridge basalt from the upwelling mantle by focused flow of melt in dunite channels. *Nature* **375**, 747–753.
- Kelemen, P. B., Hanghøj, K. & Greene, A. R. (2003). One view of the geochemistry of subduction-related magmatic arcs with an emphasis on primitive andesite and lower crust. In: Holland, H. D. & Turekian, K. K. (eds) *Treatise on Geochemistry, Vol. 4, the Crust*. Amsterdam: Elsevier, pp. 749–806.
- Kerr, A., White, R. & Saunders, A. (2000). LIP reading: recognizing oceanic plateau in the geological record. *Journal of Petrology* **41**, 1041–1056.
- Leeman, W. P. (1983). The influence of crustal structure on compositions of subduction-related magmas. *Journal of Volcanology and Geothermal Research* **18**, 561–588.
- Le Maitre, R. W. (2002). *Igneous Rocks: A Classification and Glossary of Terms: Recommendations of the International Union of Geological Sciences Subcommission on the Systematics of Igneous Rocks*. Cambridge: Cambridge University Press, 236 pp.
- Li, X. H., Li, W. X., Li, Q. L., Wang, X. C., Liu, Y. & Yang, Y. H. (2010a). Petrogenesis and tectonic significance of the 850 Ma Gangbian alkaline complex in South China: evidence from *in situ* zircon U–Pb dating, Hf–O isotopes and whole rock geochemistry. *Lithos* **114**, 1–15.
- Li, X. H., Long, W. G., Li, Q. L., Liu, Y., Zheng, Y. F., Yang, Y. H., Chamberlain, K. R., Wan, D. F., Guo, C. H., Wang, X. C. & Tao, H. (2010b). Penglai zircon megacrysts: a potential new working reference material for microbeam determination of Hf–O isotopes and U–Pb age. *Geostandards and Geoanalytical Research* **34**, 117–134.
- Li, X. H., Liu, Y., Li, Q. L., Guo, C. & Chamberlain, K. R. (2013a). Correction to ‘Precise determination of Phanerozoic zircon Pb/Pb age by multi collector SIMS without external standardization’. *Geochemistry, Geophysics, Geosystems* **10**, 573–575.
- Li, X. H., Tang, G. Q., Gong, B., Yang, Y. H., Hou, K. J., Hu, Z. C., Li, Q. L., Liu, Y. & Li, W. X. (2013b). Qinghu zircon: a working reference for microbeam analysis of U–Pb age and Hf and O isotopes. *Chinese Science Bulletin* **58**, 4647–4654.
- Liu, Y. J., Neubauer, F., Genser, J., Takasu, A., Ge, X. H. & Handler, R. (2006). $^{40}\text{Ar}/^{39}\text{Ar}$ ages of blueschist facies pelitic schists from Qingshuigou in the Northern Qilian Mountains, western China. *Island Arc* **15**, 187–198.
- Ludwig, K. R. (2003). *User’s Manual for Isoplot 3.00: A Geochronological Toolkit for Microsoft Excel*. Berkeley Geochronology Center Special Publication, **4**.
- Mann, P. & Taira, A. (2004). Global tectonic significance of the Solomon Islands and Ontong Java Plateau convergent zone. *Tectonophysics* **389**, 137–190.
- Marchesi, C., Garrido, C. J., Godard, M., Belley, F. & Ferré, E. (2009). Migration and accumulation of ultra-depleted subduction-related melts in the Massif du Sud ophiolite (New Caledonia). *Chemical Geology* **266**, 171–186.
- Médard, E., Schmidt, M. W., Schiano, P. & Ottolini, L. (2006). Melting of amphibole-bearing wehrlites: an experimental study on the origin of ultra-calcic nepheline-normative melts. *Journal of Petrology* **47**, 481–504.
- Mitchell, A. L. & Grove, T. L. (2015). Melting the hydrous, subarc mantle: the origin of primitive andesites. *Contributions to Mineralogy and Petrology* **170**, 13, doi: 10.1007/s00410-015-1161-4.
- Miyashiro, A. (1974). Volcanic rock series in island arcs and active continental margins. *American Journal of Science* **274**, 321–355.
- Morel, M. L. A., Nebel, O., Nebel-Jacobsen, Y. J., Miller, J. S. & Vroon, P. Z. (2008). Hafnium isotope characterization of the GJ-1 zircon reference material by solution and laser ablation MC-ICPMS. *Chemical Geology* **255**, 231–235.
- Nielsen, R. L., Forsythe, L. M., Gallahan, W. E. & Fisk, M. R. (1994). Major- and trace-element magnetite–melt equilibria. *Chemical Geology* **117**, 167–191.
- Niu, Y. L. (1997). Mantle melting and melt extraction processes beneath ocean ridges: Evidence from abyssal peridotites. *Journal of Petrology* **38**, 1047–1074.
- Niu, Y. L. (2004). Bulk-rock major and trace element compositions of abyssal peridotites: implications for mantle melting, melt extraction and post-melting processes beneath mid-ocean ridges. *Journal of Petrology* **45**, 2423–2458.
- Niu, Y. L., O’Hara, M. J. & Pearce, J. A. (2003). Initiation of subduction zones as a consequence of lateral compositional buoyancy contrast within the lithosphere: a petrological perspective. *Journal of Petrology* **44**, 764–778.
- Niu, Y. L., Shi, X. F., Li, T. G., Wu, S. G., Sun, W. D. & Zhu, R. X. (2017). Testing the mantle plume hypothesis: an IODP effort to drill into the Kamchatka–Okhotsk Sea basement. *Science Bulletin* **62**, 1464–1472.
- Nur, A. & Ben-Avraham, Z. (1982). Oceanic plateaus, the fragmentation of continents, and mountain building. *Journal of Geophysical Research* **87**, 3644–3661.
- Pearce, J. A. (2008). Geochemical fingerprinting of oceanic basalts with applications to ophiolite classification and the search for Archean oceanic crust. *Lithos* **100**, 14–48.
- Pearce, J. A., Kempton, P. D., Nowell, G. M. & Noble, S. R. (1999). Hf–Nd element and isotope perspective on the nature and provenance of mantle and subduction components in Western Pacific arc–basin systems. *Journal of Petrology* **40**, 1579–1611.
- Pearce, T. H., Gorman, B. E. & Birkett, T. C. (1977). The relationship between major element chemistry and tectonic environment of basic and intermediate volcanic rocks. *Earth and Planetary Science Letters* **36**, 121–132.
- Petterson, M., Babbs, T., Neal, C., Mahoney, J., Saunders, A., Duncan, R., Tolia, D., Magu, R., Qopoto, C., Mahoa, H. & Natogga, D. (1999). Geological–tectonic framework of Solomon Islands, SW Pacific: crustal accretion and growth within an intra-oceanic setting. *Tectonophysics* **301**, 35–60.
- Putirka, K. D. (2008). Thermometers and barometers for volcanic systems. In: Putirka, K. D. & Tepley, F. J., III, (eds) *Mineral, Inclusions and Volcanic Process. Mineralogical Society of America and Geochemical Society, Reviews in Mineralogy and Geochemistry* **69**, 61–120.
- Rohrbach, A., Schuth, S., Ballhaus, C., Münker, C., Matveev, S. & Qopoto, C. (2005). Petrological constraints on the origin of arc picrites, New Georgia Group, Solomon Islands. *Contributions to Mineralogy and Petrology* **149**, 685–698.
- Rudnick, R. L. & Gao, S. (2003). Composition of the continental crust. In: Rudnick, R. L. (ed.) *Treatise on Geochemistry, The Crust, Vol. 3*. Amsterdam: Elsevier, pp. 1–64.

- Saunders, A., Tarney, J., Kerr, A. & Kent, R. (1996). The formation and fate of large oceanic, igneous provinces. *Lithos* **37**, 81–95.
- Scherer, E., Munker, C. & Mezger, K. (2001). Calibration of the lutetium–hafnium clock. *Science* **293**, 683–687.
- Schiano, P., Eiler, J. M., Hutcheon, I. D. & Stolper, E. M. (2000). Primitive CaO-rich, silica-undersaturated melts in island arcs: evidence for the involvement of clinopyroxene-rich lithologies in the petrogenesis of arc magmas. *Geochemistry, Geophysics, Geosystems* **1**, doi: 10.1029/1999GC000032.
- Shimoda, G., Tatsumi, Y., Nohda, S., Ishizaka, K. & Jahn, B. M. (1998). Setouchi high-Mg andesites revisited: geochemical evidence for melting of subducting sediments. *Earth and Planetary Science Letters* **160**, 479–492.
- Sláma, J., Košler, J., Condon, D. J., Crowley, J. L., Gerdes, A., Hanchar, J. M., Horstwood, M. S. A., Morris, G. A., Nasdala, L., Norberg, N., Schaltegger, U., Schoene, B., Tubrett, M. N. & Whitehouse, M. J. (2008). Plešovice zircon—a new natural reference material for U–Pb and Hf isotopic microanalysis. *Chemical Geology* **249**, 1–35.
- Sobolev, A. V., Hofmann, A. W., Stephan, S. V. & Nikogosian, I. K. (2005). An olivine-free mantle source of Hawaiian shield basalts. *Nature* **434**, 590–597.
- Song, S. G., Zhang, L. F., Niu, Y. L., Su, L., Song, B. & Liu, D. Y. (2006). Evolution from oceanic subduction to continental collision: a case study of the Northern Tibetan Plateau inferred from geochemical and geochronological data. *Journal of Petrology* **47**, 435–455.
- Song, S. G., Niu, Y. L., Zhang, L. F., Wei, C. J., Liou, J. & Su, L. (2009). Tectonic evolution of Early Paleozoic HP metamorphic rocks in the North Qilian Mountains, NW China: new perspectives. *Journal of Asian Earth Sciences* **35**, 334–353.
- Song, S. G., Su, L., Li, X. H., Zhang, G. B., Niu, Y. L. & Zhang, L. F. (2010). Tracing the 850-Ma continental flood basalts from a piece of subducted continental crust in the North Qaidam UHPM belt, NW China. *Precambrian Research* **183**, 805–816.
- Song, S. G., Su, L., Li, X. H., Niu, Y. L. & Zhang, L. F. (2012). Grenville-age orogenesis in the Qaidam–Qilian block: the link between South China and Tarim. *Precambrian Research* **220–221**, 9–22.
- Song, S. G., Niu, Y. L., Su, L. & Xia, X. H. (2013). Tectonics of the North Qilian orogen, NW China. *Gondwana Research* **23**, 1378–1401.
- Song, S. G., Niu, Y. L., Su, L., Zhang, C. & Zhang, L. F. (2014). Continental orogenesis from ocean subduction, continent collision/subduction, to orogen collapse, and orogen recycling: the example of the North Qaidam UHPM belt, NW China. *Earth-Science Reviews* **129**, 59–84.
- Song, S. G., Yang, L. M., Zhang, Y. Q., Niu, Y. L., Wang, C., Su, L. & Gao, Y. L. (2017). Qi–Qin Accretionary Belt in Central China Orogen: accretion by trench jam of oceanic plateau and formation of intra-oceanic arc in the Early Paleozoic Qin–Qi–Kun Ocean. *Science Bulletin* **62**, 1035–1038.
- Sorbadere, F., Médard, E., Laporte, D. & Schiano, P. (2013a). Experimental melting of hydrous peridotite–pyroxenite mixed sources: constraints on the genesis of silica-undersaturated magmas beneath volcanic arcs. *Earth and Planetary Science Letters* **384**, 42–56.
- Sorbadere, F., Schiano, P. & Métrich, N. (2013b). Constraints on the origin of nepheline-normative primitive magmas in island arcs inferred from olivine-hosted melt inclusion compositions. *Journal of Petrology* **54**, 215–233.
- Stacey, J. S. & Kramers, J. D. (1975). Approximation of terrestrial lead isotope evolution by a two-stage model. *Earth and Planetary Science Letters* **26**, 207–221.
- Stern, R. A., Hanson, G. N. & Shirey, S. B. (1989). Petrogenesis of mantle-derived, LILE-enriched Archean monzodiorites and trachyandesites (sanukitoids) in southwestern Superior Province. *Canadian Journal of Earth Sciences* **26**, 1688–1712.
- Stern, R. J. (2004). Subduction initiation: spontaneous and induced. *Earth and Planetary Science Letters* **226**, 275–292.
- Stern, R. J. (2010). The anatomy and ontogeny of modern intra-oceanic arc systems. In: Kusky, T. M., Zhai, M.-G. & Xiao, W. (eds) *The Evolving Continents: Understanding Processes of Continental Growth*. Geological Society, London, Special Publications **338**, 7–34.
- Stern, R. J., Reagan, M., Ishizuka, O., Ohara, Y. & Whattam, S. (2012). To understand subduction initiation, study forearc crust: to understand forearc crust, study ophiolites. *Lithosphere* **4**, 469–483.
- Sun, S. S. & McDonough, W. F. (1989). Chemical and isotopic systematics of oceanic basalts; implications for mantle composition and processes. In: Saunders, A. D. & Norry, M. J. (eds) *Magmatism in the Ocean Basins*. Geological Society, London, Special Publications **42**, 313–345.
- Takahima, R., Nishi, H. & Yoshida, T. (2002). Geology, petrology and tectonic setting of the Late Jurassic ophiolite in Hokkaido, Japan. *Journal of Asian Earth Sciences* **21**, 197–215.
- Tang, G. J., Wang, Q., Wyman, D. A., Li, Z. X., Xu, Y. G. & Zhao, Z. H. (2012). Metasomatized lithosphere–asthenosphere interaction during slab roll-back: evidence from Late Carboniferous gabbros in the Luotuoogou area, Central Tianshan. *Lithos* **155**, 67–80.
- Tatsumi, Y. (2006). High-Mg andesites in the Setouchi Volcanic Belt, Southwest Japan: analogy to Archean magmatism and continental crust formation? *Annual Review of Earth and Planetary Sciences* **34**, 467–499.
- Tatsumi, Y. & Hanyu, T. (2003). Geochemical modeling of dehydration and partial melting of subducting lithosphere: toward a comprehensive understanding of high-Mg andesite formation in the Setouchi volcanic belt, SW Japan. *Geochemistry, Geophysics, Geosystems* **4**, 1081, doi: 10.1029/2003GC000530.
- Till, C. B., Grove, T. L. & Withers, A. C. (2012). The beginnings of hydrous mantle wedge melting. *Contributions to Mineralogy and Petrology* **163**, 669–688.
- Tung, K., Yang, H. J., Yang, H. Y., Liu, D. Y., Zhang, J. X., Wan, Y. S. & Tseng, C. Y. (2007). SHRIMP U–Pb geochronology of the zircons from the Precambrian basement of the Qilian Block and its geological significances. *Chinese Science Bulletin* **52**, 2687–2701.
- Tung, K. A., Yang, H. Y., Liu, D. Y., Zhang, J. X., Yang, H. J., Shau, Y. H. & Tseng, C. Y. (2013). The Neoproterozoic granitoids from the Qilian Block, NW China: Evidence for a link between the Qilian and South China blocks. *Precambrian Research* **235**, 163–189.
- Valley, J. W. (2003). Oxygen isotopes in zircon. In: Hanchar, J. M. & Hoskin, P. W. O. (eds) *Zircon. Mineralogical Society of America and Geochemical Society, Reviews in Mineralogy and Geochemistry* **53**, 343–385.
- Valley, J. W., Lackey, J. S., Cavosie, A. J., Clechenko, C. C., Spicuzza, M. J., Basei, M. A. S., Bindeman, I. N., Ferreira, V. P., Sial, A. N., King, E. M., Peck, W. H., Sinha, A. K. & Wei, C. S. (2005). 4.4 billion years of crustal maturation: oxygen isotope ratios of magmatic zircon. *Contributions to Mineralogy and Petrology* **150**, 561–580.
- Vervoort, J. D., Plank, T. & Prytulak, J. (2011). The Hf–Nd isotopic composition of marine sediments. *Geochimica et Cosmochimica Acta* **75**, 5903–5926.

- Villa, I. M., De Bièvre, P., Holden, N. E. & Renne, P. R. (2015). IUPAC-IUGS recommendation on the half life of ^{87}Rb . *Geochimica et Cosmochimica Acta* **164**, 382–385.
- Wan, Y. S., Xu, Z. Q., Yang, J. S. & Zhang, J. X. (2001). Ages and compositions of the Precambrian high-grade basement of the Qilian terrane and its adjacent areas. *Acta Geologica Sinica (English Edition)* **75**, 375–384.
- Wang, H., Wu, Y. B., Li, C. R., Zhao, T. Y., Qin, Z. W., Zhu, L. Q., Gao, S., Zheng, J. P., Liu, X. M. & Zhou, L. (2014). Recycling of sediment into the mantle source of K-rich mafic rocks: Sr–Nd–Hf–O isotopic evidence from the Fushui complex in the Qinling orogen. *Contributions to Mineralogy and Petrology* **168**, 1062, doi:10.1007/s00410-014-1062-y.
- Wang, T., Wang, Z. Q., Yan, Z., Ma, Z. H., He, S. F., Fu, C. L. & Wang, D. S. (2016). Geochronological and geochemical evidence of amphibolite from the Hualong Group, northwest China: implication for the early Paleozoic accretionary tectonics of the Central Qilian belt. *Lithos* **248–251**, 12–21.
- White, W. M. (2010). Oceanic island basalts and mantle plumes: the geochemical perspective. *Annual Review of Earth and Planetary Sciences* **38**, 133–160.
- Wiedenbeck, M., Allé, P., Corfu, F., Griffin, W. L., Meier, M., Oberli, F., von Quadt, A., Roddick, J. C. & Spiegel, W. (1995). Three natural zircon standards for U–Th–Pb, Lu–Hf, trace-element and REE analyses. *Geostandards and Geoanalytical Research* **19**, 1–23.
- Winchester, J. A. & Floyd, P. A. (1977). Geochemical discrimination of different magma series and their differentiation products using immobile elements. *Chemical Geology* **20**, 325–343.
- Wood, D. A. (1980). The application of a Th–Hf–Ta diagram to problems of tectonomagmatic classification and to establishing the nature of crustal contamination of basaltic lavas of the British Tertiary Volcanic Province. *Earth and Planetary Science Letters* **50**, 11–30.
- Workman, R. K. & Hart, S. R. (2005). Major and trace element composition of the depleted MORB mantle (DMM). *Earth and Planetary Science Letters* **231**, 53–72.
- Wu, F. Y., Yang, Y. H., Xie, L. W., Yang, J. H. & Xu, P. (2006). Hf isotopic compositions of the standard zircons and baddeleyites used in U–Pb geochronology. *Chemical Geology* **234**, 105–126.
- Wu, H. Q., Feng, Y. M. & Song, S. G. (1993). Metamorphism and deformation of blueschist belts and their tectonic implications, North Qilian Mountains, China. *Journal of Metamorphic Geology* **11**, 523–536.
- Xia, X. H., Song, S. G. & Niu, Y. L. (2012). Tholeiite–boninite terrane in the North Qilian suture zone: implications for subduction initiation and back-arc basin development. *Chemical Geology* **328**, 259–277.
- Xiao, W. J., Windley, B. F., Yong, Y., Yan, Z., Yuan, C., Liu, C. Z. & Li, J. L. (2009). Early Paleozoic to Devonian multiple-accretionary model for the Qilian Shan, NW China. *Journal of Asian Earth Sciences* **35**, 323–333.
- Yan, Z., Wang, Z. & Li, J. L. (2012). Tectonic settings and accretionary orogenesis of the West Qinling Terrane, northeastern margin of the Tibet Plateau. *Acta Petrologica Sinica* **28**, 1808–1828.
- Yan, Z., Aitchison, J., Fu, C. L., Guo, X. Q., Niu, M. L., Xia, W. J. & Li, J. L. (2015). Hualong Complex, South Qilian terrane: U–Pb and Lu–Hf constraints on Neoproterozoic micro-continental fragments accreted to the northern Proto-Tethyan margin. *Precambrian Research* **266**, 65–85.
- Yang, J. S., Xu, Z. Q., Zhang, J. X., Song, S. G., Wu, C., Shi, R. D., Li, H. & Brunel, M. (2002). Early Palaeozoic North Qaidam UHP metamorphic belt on the north-eastern Tibetan plateau and a paired subduction model. *Terra Nova* **14**, 397–404.
- Yang, L. M., Song, S. G., Allen, M. B., Su, L., Dong, J. L. & Wang, C. (2018). Oceanic accretionary belt in the West Qinling Orogen: Links between the Qinling and Qilian orogens, China. *Gondwana Research* **64**, 137–162.
- Yogodzinski, G. M., Volynets, O. N., Koloskov, A. V., Seliverstov, N. I. & Matvenkov, V. V. (1994). Magnesian andesites and the subduction component in a strongly calc-alkaline series at Piip Volcano, Far Western Aleutians. *Journal of Petrology* **35**, 163–204.
- Zhang, J. X., Wan, Y. S., Xu, Z. Q., Yang, J. S. & Meng, F. C. (2001). Discovery of basic granulite and its formation age in Delingha area, North Qaidam Mountains. *Acta Petrologica Sinica* **17**, 453–458.
- Zhang, J. X., Meng, F. C. & Wan, Y. S. (2007). A cold Early Palaeozoic subduction zone in the North Qilian Mountains, NW China: petrological and U–Pb geochronological constraints. *Journal of Metamorphic Geology* **25**, 285–304.
- Zhang, Y. Q., Song, S. G., Yang, L. M., Su, L., Niu, Y. L., Allen, M. B. & Xu, X. (2017). Basalts and picrites from a plume-type ophiolite in the South Qilian Accretionary Belt, Qilian Orogen: accretion of a Cambrian Oceanic Plateau? *Lithos* **278–281**, 97–110.
- Zheng, Y.-F. & Hermann, J. (2014). Geochemistry of continental subduction-zone fluids. *Earth, Planets and Space* **66**, 93, doi: 10.1186/1880-5981-66-93.